Probabilistic Tsunami Hazard Assessment (PTHA) for Southeast Coast of Chinese Mainland and Taiwan Island

Ye Yuan[1,2,3] , Hongwei Li[1] , Yong Wei[4,5] , Fengyan Shi[2] , Zongchen Wang[1], Jingming Hou[1,3], Peitao Wang[1,3] , and Zhiguo Xu[1]

[1]National Marine Environmental Forecasting Center, Beijing, China, [2]Center for Applied Coastal Research, University of Delaware, Newark, DE, USA, [3]Key Laboratory of Research on Marine Hazards Forecasting, Ministry of Natural Resources of China, Beijing, China, [4]Joint Institute for the Study of Atmosphere and Ocean, University of Washington, Seattle, WA, USA, [5]NOAA Center for Tsunami Research, Pacific Marine Environmental Laboratory, Seattle, WA, USA

Abstract A Probabilistic Tsunami Hazard Assessment (PTHA) study on the Chinese Mainland and the Taiwan Island was conducted. Characterized by broad and shallow continental shelves, the offshore region along Chinese Mainland's east coast yields a significant nonlinear effect and bottom friction to the propagating long waves. To address these shallow-water effects, a fully nonlinear Boussinesq model was used in the computation-based PTHA framework. We found that the inappropriate usage of the linear wave model could considerably overestimate the tsunami hazards along the East China Sea (ECS) and the Yellow Sea. Tsunami hazard along the coastline of Chinese Mainland is generally moderate. Elevated tsunami hazard levels are found along both flanks of the Yangtze and Pearl estuaries. The probability of these coastlines impacted by 1 m or greater tsunami waves (at 10-m isobath) is about 14%–40% in next century. The shallow and tongue-shaped submarine terrain amplifies the hazard level by trapping the tsunami energy in these areas. Major subduction zones in the Northwest Pacific were identified as the main sources of destructive events along the coast of ECS and the Taiwan Island, while the Manila Trench is the main source zone that threatens the Northern South China Sea. The tsunami hazards generated by the crustal earthquakes are modest, yet not negligible, particularly in the Taiwan Strait. We found the risk of tsunami inundation along the coast of Shanghai is low based on the hazard curves of total water level that incorporates the aleatory uncertainty of tides.

Plain Language Summary Tsunamis are infrequent yet devastating natural hazards. Most tsunami waves are generated by underwater earthquakes, and propagate onshore with transformation of wave amplitude and wave length. The Probabilistic Tsunami Hazard Assessment is a quantitative means to estimate the probability of tsunamis affecting the coastal areas of interest, with the purposes of enhancing public awareness and assisting disaster-mitigation activities. Our study aims to address the common concerns of whether the subduction zones in the Pacific Ocean and the local crustal faults may endanger China's low-lying coastal areas that are susceptible to tsunami inundation. The main finding of the study is that both flanks of the Yangtze Estuary and the Pearl Estuary possess higher levels of tsunami hazards due to their shallow and tongue-shaped submarine terrains that amplify the hazard by trapping tsunami energy. How often tsunamigenic earthquakes occur, how the earthquakes rupture, and how the generated tsunami waves propagate onshore, are subject to large uncertainties. We analyze these uncertainties in terms of a sensitivity study. In particular, for very shallow and wide East China Sea shelf, the bias introduced by tsunami modeling is significant when the wave dynamics are not modeled accurately.

1. Introduction

Tsunami impacts along the coastline of Chinese Mainland received little attention until the 2011 M_w 9.0 Tohoku earthquake and tsunami devastated the neighboring country of Japan and produced 30–60 cm wave amplitudes along the East China coasts (Figure 1). In the wake of the Tohoku event, the emergency authorities of China started to ponder how a similar event elsewhere in the Pacific Rim might affect the coastal fringe of China, where the coastal communities built on low land with hundreds of millions of residents and vast infrastructures would be devastated by severe coastal inundation. For a long period of time, the tsunami hazards in Chinese Mainland were not fully addressed due to two main reasons: a vast and shallow
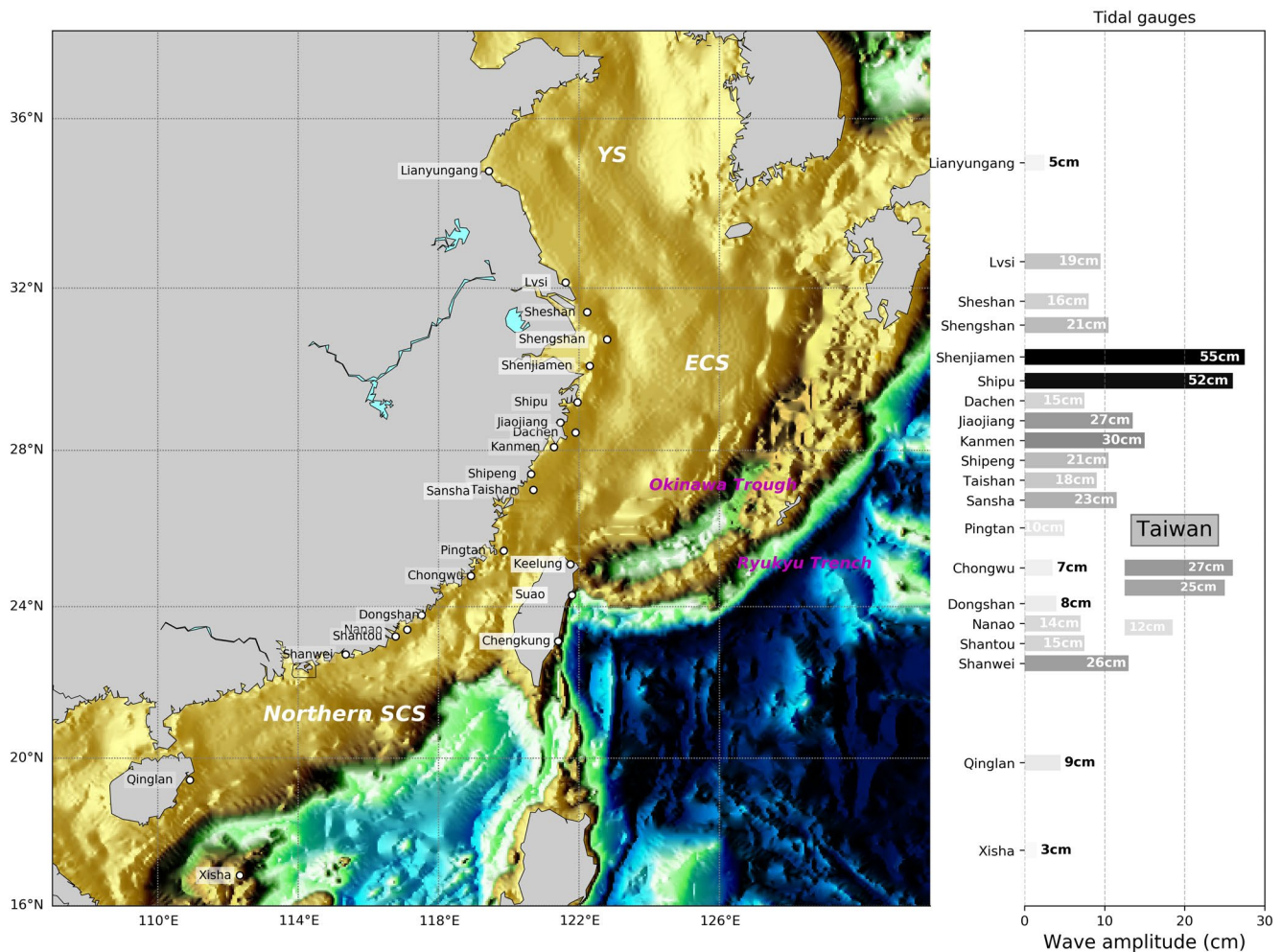
Figure 1. Maximum tsunami wave amplitude (wave crest to mean sea level) along the coasts of Chinese Mainland and Taiwan Island during the 2011 M_w 9.0 Tohoku tsunami.

continental shelf along the east coast of China that was assumed likely to dissipate most of the tsunami wave energy, and relatively low seismicity in the adjacent subduction zones, such as the West Nankai Trough, the Ryukyu Trench and the Manila Trench, in the past century. The historical tsunamis recorded along China's coasts are sparse temporally and spatially. By careful inspection, Lau et al. (2010) revealed that a majority of the historical records in the northeastern region of South China Sea (SCS) is likely to be erroneous, and only 23 of them were valid and confirmed events. Moreover, it has been difficult to differentiate the causes of coastal flooding between tsunamis and storm surges since both are sea level-related inundation processes.

Recently, a series of survey and research projects initiated in China aimed to develop tsunami inundation maps at the community level based on the worst-case scenarios. The purpose of our study is to address the common concerns about (1) which part of China's coastline will be affected by tsunamis generated from Pacific-wide and regional sources, and (2) how often the tsunami hazards might occur along these coasts with respect to different threat levels. The present study aims to provide guidance for the local emergency authorities to identify high-risk coasts for finer-scale inundation hazard assessments.

In the last two decades, we have witnessed the rapid development of the methodology of Probabilistic Tsunami Hazard Assessment (PTHA; Satake, 2014), as well as its applications globally (Davies et al., 2018; Løvholt et al., 2014). Examples include Japan (Annaka et al., 2007; De Risi & Goda, 2016; De Risi et al., 2017), Australia (Burbidge et al., 2008), southeast Asia (Horspool et al., 2014; Suppasri et al., 2012), New Zealand

(Lane et al., 2013; Power et al., 2013), United States (Geist & Parsons, 2009; González et al., 2009; Omira et al., 2015), the Caribbean (Hayes et al., 2014), Mexico (Mori et al., 2017), the Pacific coast of Central America (Zamora & Babeyko, 2019), the Mediterranean (Sørensen et al., 2012), the northwest Indian Ocean (Heidarzadeh & Kijko, 2011) and the SCS (Li et al., 2016; Li et al., 2018; Sepúlveda et al., 2019). PTHA estimates the likelihood that the tsunami wave amplitude (or inundation depth) at a particular location will exceed a given level within a certain period of time (Geist & Parsons, 2006). Compared to the worst scenario-based approach, PTHA is more effective when applied to engineering design, land-use planning and risk mitigation activities. However, considerable variability exists due to multiple sources of uncertainty associated with the PTHA framework. The main sources of uncertainty include seismicity probability, source geometry, coseismic slip distribution, and tsunami modeling approaches. Intensive efforts have been made in recent years to identify these uncertainties and incorporate them into PTHA procedures using the logic trees and Monte Carlo sampling (Grezio et al., 2017; Selva et al., 2016).

One of the key components of PTHA is the main characteristics of the seismicity (β-value) and the corner magnitude, which are used to define the Gutenberg-Richter (GR) relationship for specified seismic zones based on available earthquake catalogs. However, the enormous uncertainties of source parameters resulting from the short-history instrumental-earthquake catalogs could lead to poor estimation of the tsunami hazards. For example, the seismicity and the associated tsunami hazards were largely underestimated in the regions of Sumatra-Andaman and East Japan because no written history and instrumental records documented historic events there with magnitudes greater than 7.9 and 8.4, respectively (Satake & Atwater, 2007). Some recent studies suggested that the possibility of mega-earthquakes in the subduction zones should be quantified by taking into account both the available earthquake catalogs and the constraints of the accumulated tectonic deformation (Kagan & Jackson, 2013; McCaffrey, 2008; Rong et al., 2014). This approach is based on the assumption of the moment conservation principle that a certain part of the tectonic deformation is released by the cumulative effect of the earthquakes, and will eventually define the bolder maximum magnitudes for most of the subduction zones. In the PTHA study for West Australia, Burbidge et al. (2008) defined a GR relationship for the Sunda Arc by quantifying its contribution to the global seismicity based on the length of the seismic zone and associated plate convergence rate. They also acknowledged the universality of this GR relationship for the subduction zones in the Pacific.

Recently, a number of studies have been conducted to evaluate the contribution of the heterogeneous coseismic slip to tsunami hazards by incorporating stochastic seismic-rupturing models into the PTHA (Davies & Griffin, 2020; Davies et al., 2015; LeVeque et al., 2016; Li et al., 2016; Sepúlveda et al., 2017). These studies indicated that by adopting only the uniform-slip distribution the PTHA may underestimate the tsunami hazards by as much as 20%–60% along the coasts of the SCS and Australia. Some other studies improved the random-slip models by considering enhanced shallow slip and the curvature of mega earthquakes along the subduction zones (LeVeque et al., 2016; Scala et al., 2020). Some sensitivity analyses on the influence of source parameters (i.e., rigidity, scaling laws) on the hazard curves were also conducted (Selva et al., 2016; Sepúlveda et al., 2019).

The uncertainties associated with tsunami modeling are not negligible. Some previous studies revealed great uncertainties in the numerical simulations of tsunamis along the SCS coast (Megawati et al., 2009; Li et al., 2016; Li et al., 2018; Sepúlveda et al., 2019). In the areas featured with complex bathymetry and broad shelves, the simplified wave governing equations that neglect nonlinear, dispersive and frictional effects, or the simplified offshore-to-coast/nearshore conversion (i.e., the Green's law based on linear theory) should be used with caution.

Moreover, for the coastal areas protected by embankments and seawalls, like the east coast of Chinese Mainland where the tidal range is about 3–7 m, the annual exceedance probability of the Total Tsunami Water Level (TTWL) integrating both tsunami and tidal water levels, rather than solely the tsunami water level (TWL), plays a more important role in risk mitigation activities (i.e., land-use planning, sea-wall construction).

Presently, the PTHA studies conducted for Chinese Mainland mainly focus on the SCS coast, where the Manila Trench is regarded as the most likely source for tsunami hazards (Li et al., 2016). Ren et al. (2017) evaluated the tsunami hazards caused by eight local crustal faults along the southern coast of China. However,

no previous study has provided a comprehensive PTHA of China's coasts that considers tsunami hazards induced by both the circum-Pacific subduction zones and the local crustal sources. Furthermore, the characteristics of tsunami waves propagating over the vast East China Sea (ECS) shelf, where the width of the shelf is usually greater than 500 km, are not fully understood but are essential to the credibility of a PTHA study. The validity of the use of Green's law in PTHA is yet not clear for tsunami waves crossing the shelves of ECS and SCS.

The paper is organized as follows: Section 2 provides an overview of potential seismic sources, including the circum-Pacific subductions zones and the local crustal faults, that may pose tsunami hazards along China's coastlines. In Section 3, we investigate the evolvement of tsunami waves over the shelves of ECS and SCS using the methods of Boussinesq modeling and dispersive-wave ray tracing. Section 4 then provides a explanation of our PTHA methodology for distant and local sources. In Section 5, we present the PTHA results along the southeast coast of Chinese Mainland and Taiwan Island. The annual exceedance probability of the TWL combining tsunami and aleatory tidal levels will also be discussed in the same section. A preliminary sensitivity analysis of several major uncertainties on the tsunami hazards follows. Conclusions are presented in Section 6.

2. Potential Seismic Sources

Generally, most of the tsunamigenic earthquakes in the subduction zones can be classified as interplate and intraplate earthquakes in terms of the source locations. For the east coast of Chinese Mainland, the candidate tsunamigenic sources include both the subducting faults around the Pacific Rim, that is, the interplate earthquakes, in the far field, and the local crustal faults beneath the continental shelves, that is, the intraplate earthquakes, in the near field. Some previous water-level observations showed that both types of earthquakes posed tsunami threats to China's coasts (Ren et al., 2017; Yu et al., 2011).

2.1. Circum-Pacific Subduction Zones

Most devastating tsunamis are generated by large earthquakes around the Pacific Rim, where the Pacific plate subducts beneath the surrounding crustal plates. In this study, the circum-Pacific subduction zones and associated source geometry are mostly adopted from the PB2002 (Bird, 2003). However, it is not necessary to consider all the subduction zones as potential tsunami sources for China. For far-field tsunamis, the seismic moment, the fault orientation, and the distance from the source to the sites of interest, are the main factors contributing to the tsunami amplitudes. To be conservative, we simply place a series of synthetic M_w 9.0-earthquake scenarios in each subduction zone to examine whether they produce a significant tsunami impact, that is, whether the maximum wave amplitude is larger than 0.3 m, along the coastlines of Chinese Mainland. Our numerical results indicate that the subduction zones of New Hebrides, Tonga-Kermadec, and Central America, only produce negligible tsunami amplitudes along China's coastlines due to fault orientation, and are thus not included in the present study.

In the region Northwest Pacific, the Ryukyu Trench, and the Manila Trench are commonly regarded as the main interplate sources that likely pose serious tsunami hazards to the coastlines of Chinese Mainland and Taiwan Island. However, unlike any other typical subduction zones where great tsunamigenic earthquakes are more common, these two trenches have only shown a low level of seismicity since the instrumental earthquake catalog was established. Along the ECS shelf and coast, the earthquakes in the Ryukyu Trench may produce greater tsunami threats due to their proximity to the east coast of China and a more favorable fault orientation. The 1771 M_w 8.0 Yaeyama earthquake produced a tsunami with a maximum runup of 30 m and devastated the southern Ryukyu Islands, killing 12,000 residents. Although geological studies suggested that large earthquakes and tsunamis have repeatedly occurred in the southern Ryukyu Trench during the past 2,000 years (Ando et al., 2018), some previous seismological studies offer evidence that this trench is weakly coupled without much strain accumulation (Ito et al., 1999; Scholz & Campos, 2012). Nevertheless, a recent study showed that a significant heterogeneity exists in the interplate coupling along the Ryukyu Trench (Nakamura & Sunagawa, 2015). Some dense GPS observations revealed that the slip rate of the southern Ryukyu Trench is close to the plate convergence rate, suggesting the plate interface is

fully locked. It is estimated that M_w 8.7 earthquakes may strike at a recurrence interval of 500 years (Hsu et al., 2012; Hsu et al., 2013). Lin et al. (2014) claimed that the occurrence of a potential Sumatra-like earthquake in the southern Ryukyu Trench is also highly likely due to the similarities in their seismicity distributions and tectonic environments.

The Manila Trench is a 1,100-km-long seismic source between South Taiwan and the Mindoro Island, where the Sunda block subducts beneath the Luzon archipelago. Due to the semi-enclosed nature of the SCS basin, the Manila Trench is regarded as the only potential earthquake source zone that is able to generate basin-wide tsunamis. Although many studies consider an upper bound of M_w 9.0–9.3 as the worst-case scenario in their SCS basin-wide tsunami hazard assessments (Nguyen et al., 2014; Suppasri et al., 2012; Wu & Huang, 2009), the likelihood of such a giant earthquake in the Manila Trench is still very controversial. Previous geodetic observations indicated the state of the aseismic creeping along the Manila Trench suggested a limited capability to host a giant earthquake there (Wang & Bilek, 2014). This conclusion is partially confirmed by the fact that few earthquakes with magnitudes greater than 7.0 have occurred in this area, and a majority of the seismic moment had been released by small- and medium-size earthquakes during the past century. However, due to the short history of the instrumental earthquake records, there has been an assumption that the Manila Trench is currently experiencing a long interseismic period before it generates large earthquakes (Sieh et al., 2008). Hsu et al. (2016) showed that the occurrence of great earthquakes of M_w 8.8–9.2 in the Manila Trench is plausible. It was further supported by (Qiu et al., 2019) that the Manila Trench is capable of generating M_w 8.5+ earthquakes with a return period of 1,000 years.

The Nankai Trough, where the Philippines Sea Plate subducts underneath the Southwest Japan with an average slip rate of 44 mm a^{-1}, has been recorded to repeatedly host many M_w 8+ mega-thrust earthquakes that generated massive tsunamis. The magnitude of a future earthquake in the Nankai Trough can be as large as M_w 9.0, comparable to the size of the 2011 Tohoku earthquake, if the entire trough region ruptures during a single event (Goda et al., 2018). A M_w 9.0 Nankai earthquake can produce up to 2-m tsunami wave amplitudes along the east coast of Chinese Mainland (Shan et al., 2018).

The present study takes into consideration earthquakes generated in the 16 subduction zones around the Pacific Rim. These sources are listed and numbered sequentially in Figure 2.

2.2. Crustal Faults

The east coast of Chinese Mainland and its shelf seas are located within a stable continental intraplate region. From north to south, the three marginal seas, the Yellow Sea (YS), the ECS, and the northern SCS form the water body possessing one of the largest continental shelves in the world. Off these broad and shallow shelves, the Philippine Sea Plate subducts beneath the Eurasian continent along the Ryukyu Arc to the east. The YS, located between the Mainland of China and the Korean Peninsula, is mostly shallow and flat with an average depth of 38 m. The shallow shelf of the ECS expands up to 600-km offshore. The northern SCS and the ECS are connected through the Taiwan Strait (TS). The typical width of the continental shelf in northern SCS ranges between 100 and 300 km.

The earthquakes occurring in the crust of the overlaying plate can be tsunamigenic (Satake & Tanioka, 1999). Both the written history and tidal observations show that crustal earthquakes beneath the shelves cannot be excluded as local tsunamigenic sources. Figure 3 shows the epicenters of crustal earthquakes with magnitudes greater than 5.0 from 780 B.C. to present. Compared with that along the boundaries of active plates, the seismicity in a passive continental margin is much weaker, yet distributed more broadly. Therefore, crustal faults beneath the shelf seas have not been well mapped. Figure 3 shows the 15 crustal fault lines (red lines) identified by the Fifth Generation of Seismic Ground Motion Parameters Zonation Map of China (China National Standard GB-18306/2015). We note that these crustal fault lines are not necessarily coincident with the distribution of earthquake clusters. It is considered appropriate to identify local tsunami sources based upon the spatial distribution of historic seismicity, rather than solely relying on the existing knowledge of the fault lines—a common approach used in the PTHA for subduction zone earthquakes. We identified several earthquake belts and zones with a relatively higher concentration of earthquakes in the YS, TS, and northern SCS (Liu, 2001). More details are described as follows. It should
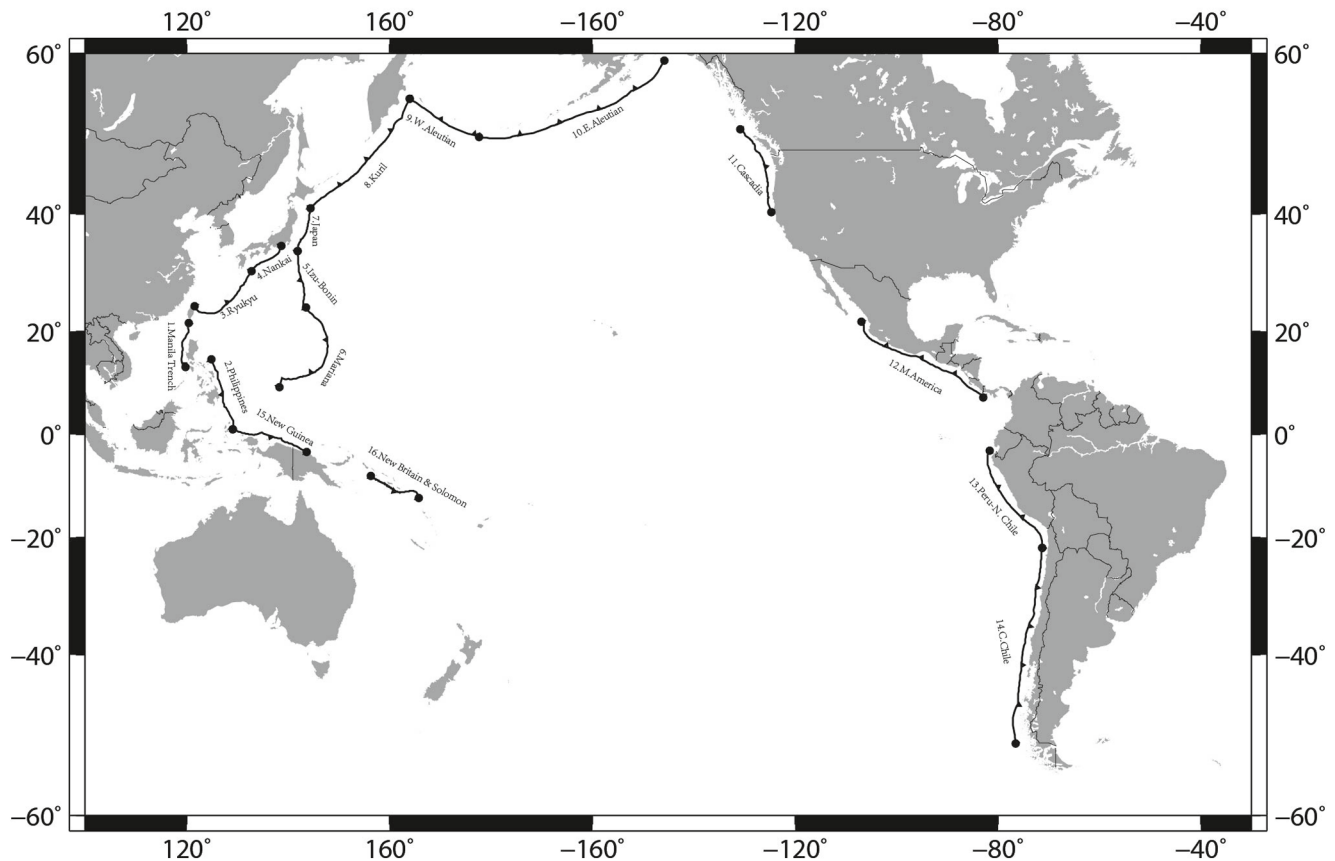
Figure 2. Circum-Pacific subduction zones identified by PB2002 plate boundaries. Starting from (1) Manila Trench, (2) Philippines Trench and moving clockwise: (3) Ryukyu Trench, (4) Nankai Trough, (5) Izu-Bonin Trench, (6) Mariana Trench, (7) Japan Trench, (8) Kuril Trench, (9) West Aleutian Trench, (10) East Aleutian Trench, (11) Cascadia Trough, (12) Middle America Trench, (13) Peru-North Chile Trench, (14) Central Chile Trench, (15) New Guinea Trench, and (16) New Britain-Solomon Trench. Both ends of each subduction zone are marked by black dots.

be noted that the PTHA study for local seismic sources in the Bohai Sea (an inland bay between 37°N and 42°N) was carried out by (Li, Wang et al., 2019), and is thus not included in the present study.

The Southern Yellow Sea Seismic Zone: Most of the earthquakes in this region are characterized by the strike-slip faulting. No record of reverse faulting has led to serious tsunami hazards in this region. The majority of the historic earthquakes have magnitudes between 5 and 7, and no credible records of serious tsunami disasters exist in this area.

The Southeast China Coastal Seismic Zone: This seismic zone starts from the TS in the north and ends at the Pearl River Estuary in the south. It coincides with the southeast China coastal fault belt, formed by the collision of the Philippine Sea and Eurasia plates. The predominant earthquake clusters are located within the TS, mainly Fujian Province and the Taiwan Southwest Shoal. The focal mechanism of a majority of the earthquakes in this region is normal faulting, a typical crustal-rupture mechanism. Historical evidence suggests that local tsunamis have been generated in this area. The 1994 M_w 6.8 TS earthquake generated a minor tsunami with the recorded wave amplitudes of 0.38 m in Penghu, Taiwan and 0.18 m in Dongshan, Fujian. The 2006 M_w 6.9 South Taiwan earthquake cut through several submarine communication cables and caused some small water-level fluctuations of 0.2–0.3 m along the west coast of Taiwan. Furthermore, the 1604 M_w 7.5–8.0 Quanzhou earthquake was believed to have generated a local tsunami in the TS (Okal et al., 2011).
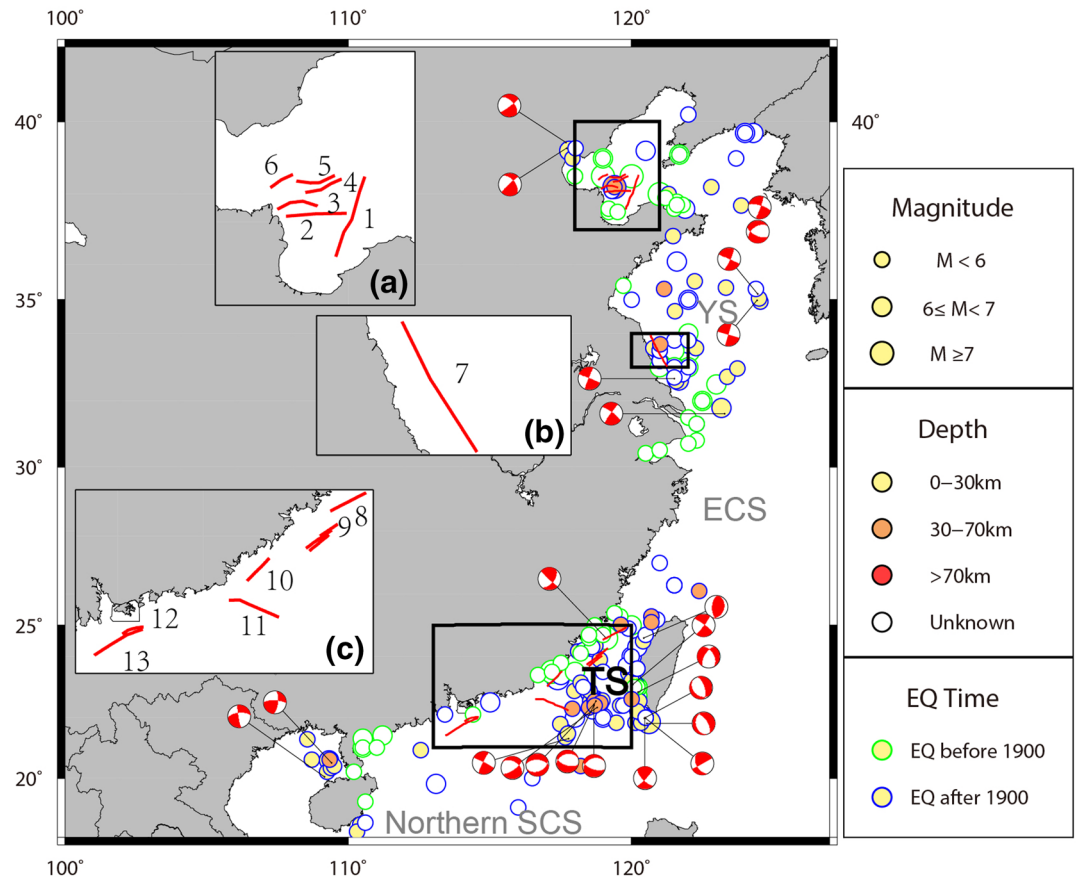
Figure 3. Distribution of historic crustal earthquakes ($M_w \geq 4.5$) and 15 crustal faults identified as potential local tsunami sources according to the fifth edition of China Seismic Ground Motion Zonation Map. The focal mechanism for major earthquakes are compiled.

3. Characteristics of Tsunami Waves Propagating Over Wide Continental Shelves

Both the ECS and the northern SCS feature wide and shallow continental shelves. In particular, the shallow shelf of ECS extends more than 500–600 km offshore all the way to the Okinawa Trough, where the water depth begins to increase moderately to 1,000 m (Figure 1). To conduct a computation-based PTHA study along China's coastlines, it is necessary to understand how tsunami waves transform over the shallow shelves of the ECS and the SCS, and how they interact with the submarine topographic features. Moreover, although the Green's law has been adopted in many PTHA studies globally and regionally to account for the wave-shoaling effect on narrow shelves (Davies & Griffin, 2020; Løvholt et al., 2014), whether it is appropriate to estimate the tsunami wave transformation over a wide continental shelf, particularly along the coasts of the ECS and northern SCS, remains poorly understood. Since the Green's law was derived from the linear wave theory, it is important to determine the extent to which the tsunami amplitudes will be overestimated if the nonlinearity, dispersion, and dissipation of the waves are neglected during the conversion of wave amplitude from offshore to nearshore. To answer this question, we use fully nonlinear Boussinesq equations to compute tsunami propagation over varying water depths of the continental shelf. Also included is a ray tracing of dispersive waves across the vast ECS shelves to investigate the effect of topographic features on tsunami propagation.

3.1. One-Dimensional Boussinesq Modeling and Amplification Factors

To include the effects of nonlinear shoaling, wave dissipation and dispersion effects, a fully nonlinear Boussinesq-type wave model FUNWAVE-TVD is adopted to describe the transformation of tsunami wave propagating over the wide continental shelf with mild slope (Kirby et al., 2013; Shi et al., 2012).

Using the latest 15-arc-sec GEBCO 2019 global relief model, we extracted a series of one-dimensional (1D) bathymetric profiles, at the grid resolutions of 200, 50, and 10 m, between the deep water and the shoreline profiles across the continental shelves of the ECS and the SCS. We configure FUNWAVE-TVD to model the propagation of tsunami waves generated by an earthquake with initial wave elevation of 2 m at the Ryukyu Trench along these transects. The bottom friction is parameterized by a roughness coefficient of 0.0025 (Li et al., 2019; Sepúlveda et al., 2019) based on the quadratic drag law. The governing equations of the FUN-WAVE-TVD can be either the fully nonlinear Boussinesq-type or nonlinear/linear shallow water equations that can be simply specified by input parameters.

As a tsunami wave propagates onshore, the variation of wave amplitude can be approximated by,

$$H = K_s \cdot K_r \cdot K_f \cdot H_0, \tag{1}$$

where H_0 and H are wave amplitudes offshore and onshore, respectively. K_s, K_r, and K_f represent the coefficients of the shoaling, refracting, and dissipating effects, respectively. For a linear wave climbing up on a planar shelf with a narrow or moderate width, Equation 1 reduces to the Green's law without considering the dissipation and the refraction (Synolakis, 1991):

$$H = K_s \cdot H_0 = \left(\frac{D_0}{D}\right)^{1/4} \cdot H_0. \tag{2}$$

Leading waves on the ECS shelf modeled by the governing equations mentioned above at the grid resolutions of 200, 50, and 10 m are presented in Figures 4a–4c, as well as in Figures S1–S4 in the Supporting Information. The numerical test using a 200-m grid shows that the initial wave heading westwards changes its waveform dramatically when it interacts with the prominent bathymetric features along the ECS transects. One can see that the water depth decreases abruptly at the Ryukyu Island-chain and the Okinawa Trough, respectively, resulting in the distinct variations of both the wavelength and the wave amplitude. The shoaling effects caused by the shelf break can be easily validated by the Green's law.

While the tsunami wave propagates further onshore, the reduction of wave amplitude due to the nonlinear effect and bottom friction becomes more evident, as shown by the red and black curves in Figure 4a. As the water depth decreases, the nonlinear and friction effect is intensified until it gradually balances out and eventually dominates the shoaling process, resulting in the decrease of wave amplitude. Figure 4a shows the wave amplitude drops to 1.2 m when approaching the coastline, and climbs up to 3 m during the runup process. In contrast, the modeling result of the linear shallow water equations (LSWE; blue line) is barely changed after the wave propagates over a long distance on the shelf.

Figures 4a–4c and S1–S4 allow us to summarize as follows the main characteristics of wave transformation over the broad ECS shelf.

1. A shoaling tsunami wave becomes increasingly asymmetry as the water depth decreases. Unlike the LSWE, the nonlinear shallow water equations (NSWE) is able to provide more accurate approximation of the front-face steepening of the leading wave.
2. Using a grid resolution of 200 m, a steady decrease of the wave amplitude during shoaling can be observed in both Boussinesq and NSWE models. It suggests the nonlinearity and bottom dissipation play predominating roles in tsunami wave reduction over the ECS shelf.
3. While both Boussinesq and NSW equations give similar modeling results at coarse grid resolution, the leading waveform exhibits more complex characteristics when refined grid sizes of 50 and 10 m are used.
4. Close to the nearshore region, the front face of the leading wave becomes so steep that it gradually disintegrates into undular bores riding on top of the main wave. These bores are featured with shorter
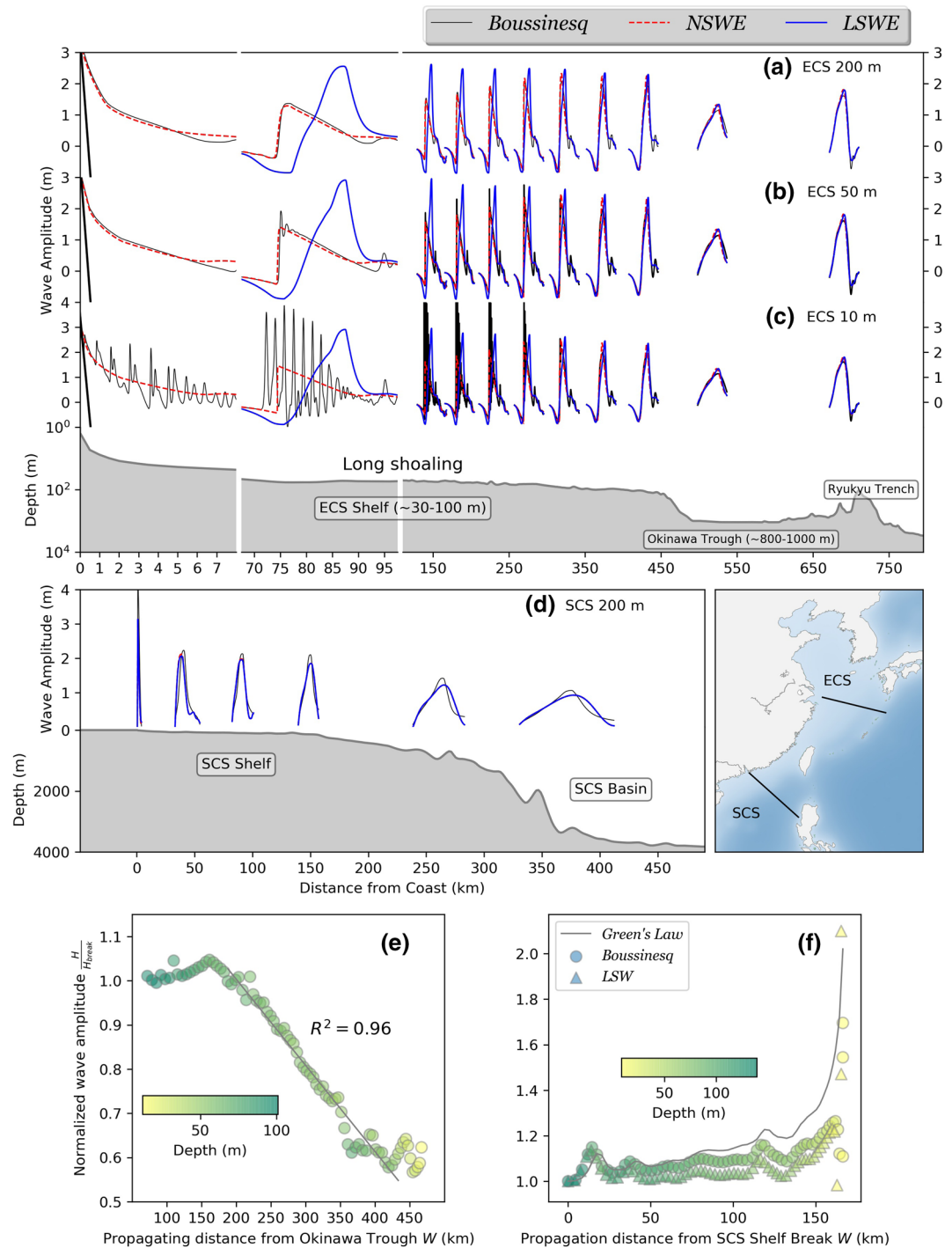
Figure 4. One-dimensional tsunami wave propagation along the ECS (a–c; corresponding to grid resolutions of 200, 50, and 10 m) and SCS (d) transects, modeled by LSWE (blue), NSWE (red) and Boussinesq Equation (black), respectively. Evolution of normalized wave amplitude along the transects of the ECS and SCS shelves is shown in (e) and (f). For the SCS shelf (f), the initial tsunami wave amplitudes modeled by Boussinesq Equations and LSWE are marked by circles and triangles, respectively; and the black line represents the shoaling factor K_s estimated by the Green's law. ECS, East China Sea; LSWE, linear shallow water equations; NSWE, nonlinear shallow water equations; SCS, South China Sea.

wavelength and larger amplitude, and gradually evolve to the form of solitons when propagating further onshore, where wave dispersion also starts to play a role (Madsen et al., 2008).

5. The amplitude of an undular bore decreases when it approaches the coastline due to wave breaking effect. Both the Boussinesq and the NSWE models give tsunami runup up to 3 m. The potential energy when maximum runup occurs can be computed by $1/2\rho gH^2$, where H is wave amplitude (Zhao et al., 2016). Here, the hydrostatic potential energy of the water beneath the still water is omitted. By integrating over the entire period of the leading wave, both the Boussinesq and NSWE models give comparable estimates, which implies the onshore energy flux could also be similar.

The maximum wave amplitude is commonly used as the main indicator for a regional tsunami hazard assessment. However, introducing the undular bore to the subsequent analysis undoubtedly further complicates the PTHA study. Tsunami damages mainly come from inland inundation processes, which is directly related to the tsunami volume and energy fluxes. As Madsen et al. (2008) noted that, although the short waves may have a local additional effect on wave impact on coastal structures, they would play hardly any role for the runup and inundation caused by the main and much longer tsunami. Here we employ modeling results obtained from the 200-m grid resolution in the subsequent analysis based on our Argument 5 above.

For a regional tsunami hazard study, the Green's law is commonly adopted to relate offshore amplitude to its nearshore counterpart. However, we show that it is not valid for the ECS shelf and can largely overestimate the tsunami hazard. For simplicity, we use the factor $K = K_s \cdot K_r \cdot K_f$ to integrate all the shoaling coefficients in Equation 1. In the current transect, K is only about 0.60 if the offshore and nearshore wave amplitudes (H_0 and H) are sampled at 100 and 10-m isobaths, respectively (Figure 4e). Actually, the factor K is site-specific as the cross-shore distance between each output point and the shelf break varies. The K values along the coastlines of the ECS can serve as substitutes for the conversion coefficients of the offshore-to-nearshore wave amplitudes used in the PTHA study as described in the following sections.

A simple approach to estimate K is illustrated in Figure 4e. H_{break} is defined as the wave amplitude at the entrance of the ECS shelf where the water depth is about 100–150 m. The normalized wave amplitude H/H_{break} is, in principle, a measure of the wave amplification or reduction when the water depth decreases. The subplot clearly suggests a linear reduction of the amplitude of the wave when it propagates onshore. The best-fit line between the normalized wave amplitude and the propagating distance from the western flank of the Okinawa Trough (W_{shelf}) gives,

$$
\begin{aligned}
K &= \left(\frac{D_0}{D}\right)^{1/4}, \text{if } W_{shelf} < 200 \ km \\
K &= 1 - 0.0021 \times (W_{shelf} - 200), \text{if } 200 \ km \leq W_{shelf} < 400 \ km,
\end{aligned}
\tag{3}
$$

where W_{shelf} also can be interpreted as the shelf width. The shelf width-value are measured from the western flank of the Okinawa Trough at depth of 120 m for the ECS shelf, and the shelf break at 300 m for the SCS shelf, respectively. For a shelf width less than 200 km, the variation of wave amplitude can be described by the Green's Law as the shoaling effect is dominant.

The shelf width of the northern SCS is smaller than that of the ECS. The cross-shore distance of the shelves in the northern SCS ranges between 150 and 300 km before the water deepens in the basin. For an earthquake with initial wave amplitude of 2 m in the Manila Trench, the leading tsunami wave arrives at the shelf break of the northern SCS in less than half hour. As suggested in Figure 4d, the wavefront steepens and its wavelength shortens during the shoaling process. The modeling results of the LSW equations (blue lines) are basically similar to those of the Boussinesq Equations, meaning LSW theory is probably adequate to describe wave propagation over the shelves in the northern SCS. Figure 4f validates the use of the Green's law in the northern SCS as it demonstrates a similar trend following the model results. We thus conclude here that, for the shelves in the ECS and the northern SCS, 200 km can be regarded as a critical width of the shelf. For a shelf wider than 200 km, the Green's law becomes less valid, and the factor K that we proposed in this section is a more rational choice for the offshore-to-nearshore wave-amplitude conversion. We thus calculated K values for each of the segments along the coastline. It is worth noting that, for shelf width less than 200 km, the K values are exactly the same as the Green's law.
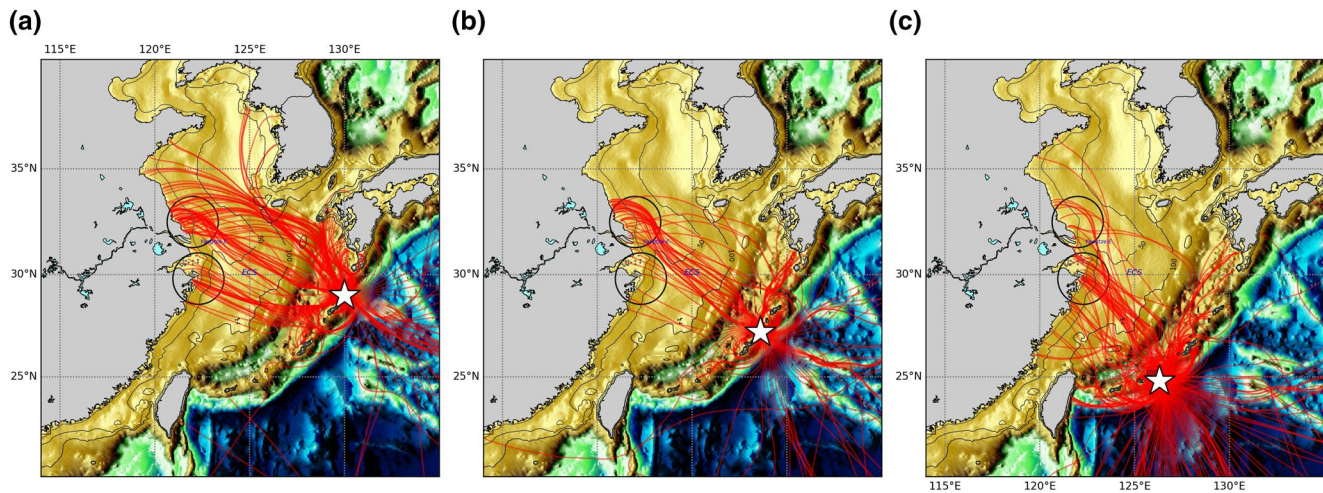
Figure 5. Ray tracing of tsunami scenarios propagating over the wide ECS shelf. The three hypothetic point-like sources are placed along the Ryukyu Trench from (a) Tokara Strait to (c) Miyako Strait. The northern and southern flanks of the Yangtze Estuary, coinciding with two tsunami-energy spots, are marked by two black circles. ECS, East China Sea.

3.2. Ray Tracing of Tsunami Wave Propagation Over the Continental Shelf

As shown in Figure 1, the TWLs extracted from tidal gauges vary considerably along the coastlines of the ECS. Although the shelf is narrower in the southern part of this coast (between the TS and Shipeng in Figure 1), the observed amplitudes there are smaller than those in the north (i.e., at the gauges of Shipu and Shenjiamen). Figure S5 in Supporting Information of this paper shows the maximum tsunami wave amplitudes in the ECS resulting from the hypothetic mega-earthquakes in the Central Chile, the Philippine Trough, and the Nankai Trough. The simulations are carried out by a 2-arc-minute transoceanic tsunami model based on the Cornell Multigrid Coupled Tsunami model (COMCOT) governed by the NSWE. One can clearly see larger wave impact along the northern part of the coasts of ECS. A noteworthy feature is the energy focusing on both flanks of the Yangtze Estuary, resulting from the bathymetric features interfering with propagating waves.

For dispersive tsunami waves, the spatial distribution of tsunami amplitudes can be better explained by the theory of ray tracing (Munk et al., 1988; Sandanbata et al., 2018). For brevity, details on ray equations of tsunami waves are summarized as Text S1 in the Supporting Information.

To its east, the ECS is bounded by the Ryukyu Islands, which extend more than 2,000 km southwestward from Kyushu, Japan, all the way to the Taiwan Island. This island chain is separated by several channels and straits, among which the Tokara Strait and the Miyako Strait form the main entrances for Pacific-wide tsunamis to penetrate the ECS. Here we place three hypothetical tsunami sources at the Tokara Strait, the Miyako Strait, and the gap in between (27°N; Figure 5). For the tsunami source at the Tokara Strait (Figure 5a), the ray-tracing results show that the ray trajectories going through the Ryukyu Islands travel mainly along three paths. Initially trapped in the Ryukyu Islands, the northernmost group of the waves first propagate northwards, and then bend their paths over the shelf via the deep channel off the southern tip of the Jeju Island. The northernmost ray group gradually alters its direction over the shallow area of the Yangtze Estuary, and finally merges with the middle ray group at the northern flank of Yangtze Estuary. This explains one of the tsunami energy-focusing point between 32° and 33°N. The other energy-focusing spot at 30°N can be explained by the southernmost ray group concentrating at the southern flank of the Yangtze Estuary. For tsunami sources at 27°N and the Miyako Strait, their ray trajectories also indicate the energy focus at both the northern and southern flanks of the Yangtze Estuary.

The interaction of impinging tsunami waves with the bathymetric features over the shelf redistributes tsunami energy in the forms of focusing and scattering. Our ray-tracing analyses clearly show the paths of tsunami waves over the shelf of the ECS conform to historic records (Figure 1), that is, the northern coast

of the ECS (Yangtze Estuary) is susceptible to higher tsunami amplitudes. Furthermore, a similar spatial distribution of the tsunami energy can be observed along the coasts of ECS for all distant tsunamis after they pass through the Ryukyu Islands. This important conclusion will be used to further explain the tsunami hazard maps in Section 5.3.

4. PTHA Methodology Applied to Subduction Zones and Crustal Faults

For study areas lacking of a complete and credible written history of tsunamis, the computation-based PTHA provides an alternative tool to evaluate the tsunami hazards. The PTHA assumes the events with tsunami amplitudes exceeding a certain specified value follow the stationary, or time-independent, Poisson process. (Geist & Parsons, 2006, 2009). The probability of at least one tsunami event with wave amplitude at coast exceeding a specified level ζ_i for a series of seismic sources during a period of time t is

$$P(\zeta > \zeta_i) = 1 - e^{-t/\tau_i}, \tag{4}$$

where τ_i is the combined recurrence interval (or recurrence rate, $1/\tau$) of tsunami amplitude equal to or greater than a specific level ζ_i for all seismic sources at the sites of interest.

The PTHA framework based on the Monte Carlo resampling is summarized in Figure 6, with details provided in Sections 4.1–4.6.

4.1. Earthquake Catalogs and Seismic Zoning

The earthquake catalog employed in the present study is the 1900-present Centennial Catalog (Storchak et al., 2013). This catalog includes all magnitudes 7.0 or larger prior to 1930, 6.5 or larger during the period 1930–1963, and 5.5 or larger during the period of 1964-present. Here, we consider the events with magnitudes greater than 6.5 since 1930. Only the shallow earthquakes with focal depths ≤70 km are considered.

Instead of using Flinn and Engdahl (F-E) polygons, we use the plate boundary model of PB2002 and the 3D geometry model Slab 2.0 together (Bird, 2003; Hayes et al., 2018) to define the subduction zones. We divide some of the subduction zones into multiple segments to accommodate the changing fault orientations, which are crucial to determine the directions of tsunami propagation (i.e., West and East Aleutian Trench, North and Central Chile Trench).

Historical earthquakes along the east coast of China from 1900 are obtained from various sources. *The Catalogue of Chinese Historical Strong Earthquakes* (Min et al., 1995) collected 1,034 earthquakes with $M_s \geq 4.7$ occurred in China from 2300 B.C. to A.D. 1911. *The Catalogue of Chinese Present Earthquakes* (Wang et al., 1999) documented the earthquake events with $M_s \geq 4.7$ from 1912 to 1990, including those in Taiwan and other nearby areas. Another main catalog, produced by the China Earthquake Network Center, contained most of the instrumentally recorded earthquakes that had occurred in China and surrounding areas since 1970. To be consistent, we converted the earthquake magnitudes from M_s and other magnitude scales to the moment magnitudes M_w using the regression relationships defined by Cheng et al. (2017). The subcatalogs for the Southern YS Seismic Zone and the Southeast China Coastal Seismic Zone are both extracted from the above-mentioned catalogs. We should point out that some of the inland earthquakes are retained in order to meet the minimal requirement for the magnitude-frequency regression in each seismic zone.

4.2. Magnitude-Frequency Distribution

The tapered Gutenberg and Richter (TGR) magnitude-frequency relation is expressed as (Bird & Kagan, 2004; Kagan, 1997),

$$F(M) = \left(\frac{M_t}{M}\right)^{\beta} \cdot exp\left(\frac{M_t - M}{M_c}\right) \; for \; M_t \leq M < \infty, \tag{5}$$
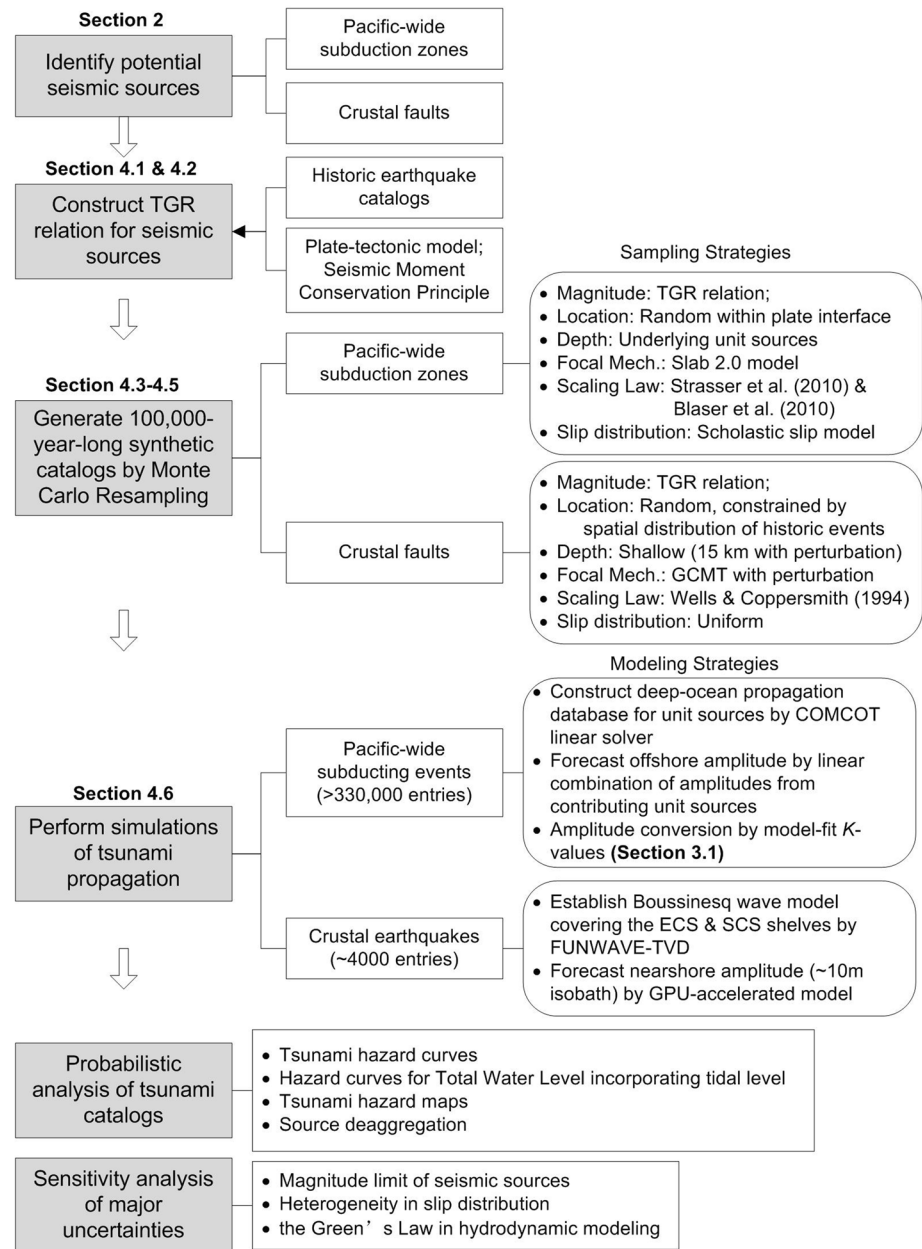
Figure 6. Flowchart of the PTHA framework based on the method of Monte Carlo resampling in the study. PTHA, Probabilistic Tsunami Hazard Assessment.

where the seismic moment M (N·m) is defined as $M = 10^{1.5m+9.0}$, $N(m)$ is the annual probability of the earthquakes with moment magnitudes larger than M, β denotes the slope of TGR distribution within the small-to-moderate moment range, M_t is the minimum seismic moment to be considered in a catalog, M_c is the corner moment where the TGR distribution begins to taper (corresponding to corner magnitude m_c). $F(M)$ is rate of the earthquakes with moment magnitudes larger than M, normalized to a cumulative rate of 1 at the threshold seismic moment M_t.

4.2.1. The Seismic Moment Conservation Principle for Subduction Zones

We construct the TGR distribution using the subcatalog of each seismic zone based on the Maximum-Likelihood method (Kagan, 1997; Rong et al., 2014). Theoretically, the TGR parameters β and M_c can be

Table 1
Parameters Related to the TGR Relationship, Source Geometry, and Plate Dynamics Among Circum-Pacific Subduction Zones

Subduction zones	N^a (≥6.5)	β	m_c^b	L (km)	W^c (km)	χ^d	$\overline{u}^e\ (mm \cdot y^{-1})$	$m_{c,T}^f$
Manila Trench	27	0.41	7.50	1,061	98	0.4	80.0	8.54
Philippines Trench	70	0.58	7.73	1,364	80	0.5	103.2	8.85
Ryukyu Trench	37	0.54	7.50	1,126	116	0.3	87.0	8.79
Nankai Trough	27	0.46	8.23	762	124	1.0	50.3	8.88
Izu-Bonin Trench	22	0.64	7.90	1,128	95	0.4	54.0	9.33
Mariana Trench	24	0.42	7.66	2,513	89	0.5	42.7	8.81
Japan Trench	112	0.50	9.16	793	162	1.0	92.2	8.73
Kuril Trench	174	0.55	8.90	2,223	130	0.8	85.6	8.96
West Aleutian Trench	30	0.39	7.50	1,058	90	0.5	74.2	8.47
East Aleutian Trench	151	0.65	9.33	2,714	107	1.0	59.9	9.46
Cascadia Trough	29	0.50	7.50	1,415	127	1.0	39.6	9.22
Middle America Trench	130	0.41	7.83	3,120	111	0.6	59.2	8.41
Peru-Chile Trench	50	0.35	8.20	2,503	124	0.8	69.6	8.85
Central Chile Trench	120	0.51	9.63	3,505	148	1.0	59.9	9.29
New Guinea Trench	80	0.49	7.80	1773	111	0.7	48.1	8.56
Solomon	85	0.49	7.86	1,177	75	0.7	94.4	8.45

[a]N is the number of events with $M_w \geq 6.5$ in 90.5 years from 1930 to present. [c]The values of down-dip width W are evaluated by Herrendörfer et al. (2015). [d]The values of seismic coupling coefficient χ are based on the GEM database. [b]m_c is derived from the maximum-likelihood estimation of TGR relation. [e]The values of plate velocity $\overline{u}$ are retrieved from the PB2002 (Bird, 2003). [f]$m_{c,T}$ is derived from the seismic moment conservation principle.

well-estimated by this approach if the subcatalogs comprise both the small and moderate events fitting a homogeneous distribution and the large ones that can well define the upper limit of the earthquake sizes. The constructed TGR distributions for the major subduction zones is presented in Supporting Information Figure S6 as blue curves, which are generally consistent with the available subcatalogs for each source. However, the log-likelihood contours in Figure S7 do not close in the direction of positive m_c. That is, due to the lack of mega earthquakes, the catalog data alone provide no useful upper limit to the corner magnitude, a critical parameter in the PTHA (Bird & Kagan, 2004; Kagan & Jackson, 2013).

In Table 1, the β-values and the corner magnitudes for all the 16 circum-Pacific subduction zones are listed in columns 2–3. The corner magnitude estimated with maximum-likelihood method (m_c for the 16 subduction zones varies between 7.5 and 9.6. For the subduction zones that have experienced earthquakes with magnitudes 9 or larger, the m_c-values range between 8.9 and 9.6. However, for other subduction zones, most of the m_c-values are below 8.0. Taking the Cascadia Subduction Zone as an example, although the turbidite records suggest a M 9.0 earthquake has a return period of 500 years, the maximum-likelihood estimate of the m_c is only 7.5 due to the lack of large earthquakes in the instrumental catalog (Rong et al., 2014). This is the case for Manila Trench and Ryukyu Trench.

Zöller (2013) also proved that the maximum likelihood estimation of the m_c can be biased in strongly undersampled models. Additional data from tectonics are needed to better constrain the magnitude limits. To deal with this issue, the principle of the seismic moment conservation was introduced to further constrain the m_c in the TGR relation. The basic assumption is that a certain part of the tectonic deformation is released by the cumulative effects of earthquakes. Including the integral form of TGR distribution and the tectonic moment rate, the corner moment $M_{c,T}$ (we add the subscript T here to avoid the confusion with M_c) can be estimated as (Rong et al., 2014),

$$M_{c,T} = \left[\frac{\chi \dot{M}_T (1-\beta)}{\alpha_t M_t^\beta \Gamma(2-\beta)} \right]^{1/(1-\beta)}, \tag{6}$$

where χ is the seismic coupling coefficient, α_t is the occurrence rate of earthquakes above the threshold moment M_t, the operator Γ denotes the gamma function, and $\dot{M}_T = \mu W L \bar{u}$ is the tectonic rate of seismic moment release from the plate-motion models. Here, μ is the rigidity set to 49 GPa (Kagan & Jackson, 2013), W is the down-dip width of the rupture fault, L is the length along the plate boundary, and $\bar{u}$ is the plate convergent rate per year. In Table 1, we summarize the seismological and geometric parameters to estimate the corner magnitude $M_{c,T}$ for all 16 subduction zones.

In Figure S6, the TGR curves by substituting the M_c with $M_{c,T}$ is plotted as red lines. The deviation of the red curves from the maximum likelihood-regressed curves (blue) is obvious at high-magnitude end, especially for those subduction zones with few mega earthquakes (i.e., Ryukyu Trench, Manila Trench, Cascadia Trench). Table 1 shows the corner magnitudes obtained using the maximum-likelihood method (m_c) and the principle of moment conservation ($m_{c,T}$). The mean values of m_c and $m_{c,T}$ are 8.1 and 8.9, respectively. The average value of $m_{c,T}$ from Rong et al. (2014) is 9.0. We attribute this minor discrepancy to different choices on earthquake catalogs, zonation, and more importantly, the way to estimate tectonic moment rate $\dot{M}_T$ in Equation 6. Rong et al. (2014) calculated tectonic moment rates for each source based on the geodetic strain rate map by Kreemer et al. (2003).

The $m_{c,T}$-value for the Japan Trench are smaller than the corresponding m_c-value by 0.5. Using Equation 5, the return period for a $M \geq 9.0$ event is 1,225 years. Usami et al. (2018) suggested a supercycle of giant earthquakes along the Japan Trench existed at a recurrence interval of 700 years based on the sand deposit records. The A.D. 869 Jogan Earthquake is believed to generate a similar tsunami as Tohoku event, and its minimum moment magnitude is estimated to be 8.6 (Namegaya & Satake, 2014). Using the parameter values for the TGR moment-frequency distribution listed in Table 1, we estimate the number of $M \geq 9.0$ events expected to occur Pacific-wide over a century is 3.4, which is slightly less than the 4 $M \geq 9.0$ events registered during the past 100 years. It should be noted that the subduction zones of New Hebrides, Tonga-Kermadec, and Central America are excluded from this study. In Section 5.4, both estimates of the corner magnitude are used to demonstrate that magnitude limits of the subduction zones are one of the first-order uncertainties in the PTHA study.

4.2.2. Crustal Earthquakes

As shown in Figure 3, the crustal earthquakes are unevenly clustered beneath the continental shelves of the Southern YS, the Northern SCS, and the TS. We truncate the entire region of the east coast of China into three seismic zones for our TGR regression analysis. The best-fit values of the seismicity slope β and the corner magnitude m_c for South YS, Northern SCS, and TS are (0.59, 7.5), (0.70, 7.2), and (0.58, 7.8), respectively.

4.3. Source Geometry and Scaling Relationship

The tsunami model used in our PTHA study is initialized with parameters defining the source geometry. For subduction zones, the commonly accepted methodology is to divide interplate slabs into many rectangular unit-sources with dimensions of 100 km along-strike and 50 km down-dip. Synthetic earthquakes can then be mapped as a number of concatenated unit-sources covering the rupture area estimated by appropriate magnitude-area scaling laws. For source geometry of each unit source, we obtained the strike and dip angles of each unit source through interpolation from the Slab 2.0 grid, while the rake angle is fixed to 90° to be conservative. The maximum depths of the seismogenic zones are taken from the Global Earthquake Model (GEM) database (Christophersen et al., 2015). Gica et al. (2007) showed that, within a reasonable range of uncertainty, the rake, dip, and focal depth only play secondary roles in tsunami waves at distant coastlines.

For crustal earthquakes occurring beneath the continental shelf along China's coastlines, the focal mechanisms exhibit high variability, and most are strike-slip and normal faults. The previous study of Ren

et al. (2017) on local tsunami hazards in the northern SCS region assumed all the crustal faults are pure thrust. However, this assumption may overestimate the contribution of local sources to the tsunami hazards. We divided each of the three seismic zones, namely the southern YS zone, the northern SCS zone, and the TS zone, into a series of 3° × 3° grids and assigned the strike, dip, and slip angles to each grid. For grids with higher seismicity, these parameters were resampled from the Gaussian distributions with the pairs of (μ, σ) determined from the historical events. For grids without enough historical records, the mean values of strike, dip, and slip angles are estimated based on the isobath orientation and the historical events over the entire seismic zone. It is worth noting that all the crustal earthquakes are treated as shallow events, and the focal depth of each grid is set to 15 km with a standard deviation of 10 km.

Another uncertainty of the PTHA came from the selection of the magnitude-length/area scaling laws when we mapped the earthquakes onto the unit-sources and computed the seafloor deformation using Okada (1985). Stirling et al. (2013) recommended that one should choose a scaling relationship compatible with the tectonic regime of interest. For the Pacific-wide sources, we employed two scaling laws (Blaser et al., 2010; Strasser et al., 2010) that are suitable for the subducting earthquakes, with each randomly assigned the synthetic events with the probability of 0.5. The rupture length and width of the crustal earthquakes are determined by relations in Leonard (2014) for stable continental region.

4.4. Stochastic Slip Model

Some recent mega earthquake and tsunami events in the Pacific provided compelling evidences that heterogeneous slips along the slab interface, particularly when involving large shallow slips, are able to produce much higher tsunami runup in the near field. Many global or regional PTHA studies treat the earthquakes as an array of unit sources with uniform, variable, or random slips based on the seismic moment. Recent studies raised concerns about whether stochastic models give practical slip distributions of a typical subducting earthquake (LeVeque et al., 2016; Scala et al., 2020), and how these slip models can produce a realistic distribution of hypothetical tsunamis (An et al., 2018; Davies, 2019). In this study, we used the random field model developed by Mai and Beroza (2002) to generate the stochastic slip distribution once the source rupture length L and width W are obtained using the scaling laws. This model describes the slip distribution using an autocorrelation function (ACF) parameterized by the correlated rupture lengths in both the strike and down-dip directions. The synthetic slip distributions for an earthquake catalog can be achieved by random selection of the ACF phase constants.

To better accommodate the source heterogeneity, we further divided the 100 × 50 km unit-sources along the Pacific Rim into subunit-sources of 20 × 10 km. These subunit-sources were used in the random slip model and then integrated back to their parental 100 × 50 km unit sources to obtain a heterogeneous slip distribution for every earthquake scenario. For a M_w 8.5 scenario in the Ryukyu Trench, we discretized the rupture area of 600 × 100 km into 12 unit sources (100 × 50-km each). Figure S8 in the Supporting Information illustrates the striking difference of the tsunami amplitudes offshore due to uniform and heterogeneous slip distributions. The tsunami amplitudes produced by the nonuniform slip distribution are remarkably larger than those resulting from the uniform slip distribution. We, therefore, considered the slip distribution as one of the aleatory uncertainties, and applied the random slip model to generate a synthetic catalog of scenarios for each subduction zone. The sensitivity analysis of tsunami hazards due to stochastic slips will be provided in Section 5.4.

4.5. Generation of Synthetic Catalogs of Earthquake Scenarios

We generated synthetic catalogs to specify the earthquake parameters, for example, event location, focal depth, magnitude, and source geometry (including the focal mechanism and the rupture dimensions), which are needed for subsequent tsunami modeling. These synthetic catalogs should also include many events for robust estimates of tsunami hazards for desired return periods. It is well-known that the Monte Carlo simulation can generate a large amount of samples that allow consideration of multiple sources of uncertainties. In this study, we adopted the open-source toolbox, EQHAZ, to perform the Monte Carlo
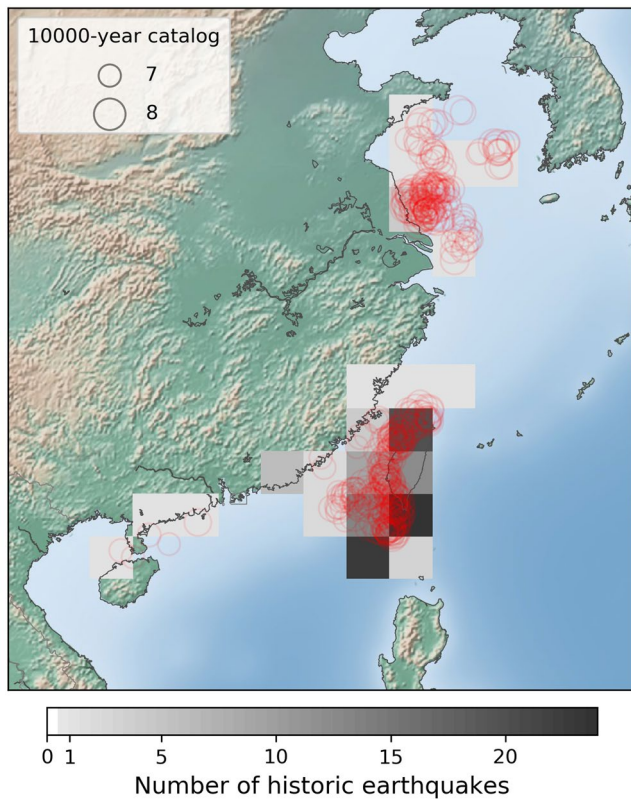
Figure 7. Heatmap of historic crustal earthquakes on the ECS and SCS shelves, overlapped with 10,000-year synthetic catalog with magnitude larger than 7 (semitransparent circle). ECS, East China Sea; SCS, South China Sea.

sampling using prescribed TGR parameters (threshold seismicity level N_0, β-value, and corner magnitude m_c) for all circum-Pacific subduction zones (Assatourians & Atkinson, 2013).

For subduction zones covered by unit sources, the earthquake locations were randomly generated following the fault orientation, and the depth and focal mechanism were then chosen from the underlying unit sources. The two scaling laws were chosen randomly with a weight of 0.5 for each to determine the rupture length and width of an earthquake scenario. Table 1 gives a suite of seismological and geometric parameters used in the Monte Carlo sampling.

For crustal source zones that are defined by polygons, event locations were determined from the spatial distribution of the historical event. The source polygon was discretized into a grid mesh with variable weights assigned to different grid points. The weights were computed from the spatial density of historical events to control the chance of each grid point being selected as the initial location of synthetic events (Assatourians & Atkinson, 2019). The benefit of this approach is to make the locations of synthetic scenarios mimic the event clustering observed from the historic catalog. Figure 7 shows that the uneven distribution of synthetic earthquakes over the shelf regions of China is consistent with the historical earthquake clusters in the southern YS and TS. The event depth and focal mechanism of each scenario are determined by random resampling from the Gaussian distribution with the (μ, σ) pairs given by Section 4.3. Using the methods stated above, we generated a 100,000-year-long earthquake catalog inclusive of the 16 subduction zones in the Pacific and the three crustal source zones for our subsequent tsunami modeling. As a results, this synthetic catalog contains more than 330,000 event entries with magnitudes above 7.5 along the plate interfaces and 3,936 crustal events with magnitudes greater than 7 across the continental shelves of the east coast of China.

4.6. Tsunami Modeling

4.6.1. Pre-computed Propagating Database for Far-Field Events

Because of the linearity of the tsunami generation/propagation, a progressing tsunami event can be quickly synthesized using the linear combination of precomputed tsunami propagation from contributing unit sources (Titov et al., 2005; Tang et al., 2008; Wei et al., 2013, 2014). This method can provide the offshore tsunami amplitudes quickly without requiring a basin-wide model simulation for every event entry in the catalog. We use the tsunami model COMCOT v1.7 to simulate the basin-wide tsunami propagation for each unit source with its linear solver. COMCOT has been extensively validated against analytical solutions and real tsunami events (Wang & Liu, 2006). The coseismic vertical displacement resulting from 1-m slip on each unit-source is obtained using the Okada's elastic half-space model (Okada, 1985).

In Supporting Information, Figure S9 presents an overview of the database of unit sources constructed for this study. The Digital Elevation Model is obtained from the ETOPO1 global relief model, which is resampled to a grid resolution of two arc min (3.7 km). The computation domain is 99°E-60°W, and 70°S-70°N. The duration of Pacific-wide simulation takes 36 h. For unit sources in the Northwest Pacific Ocean, the simulation duration is 18 h.

For model outputs, we selected a total of 256 offshore points over the 50-m isobath (triangles in Figure 8) along the coast of Chinese Mainland, except for the north of Jiangsu where the average water depth offshore is only about 30 m. The offshore points along the east coast of Taiwan Island have larger water depths between 50 and 300 m due to the narrower shelf there.
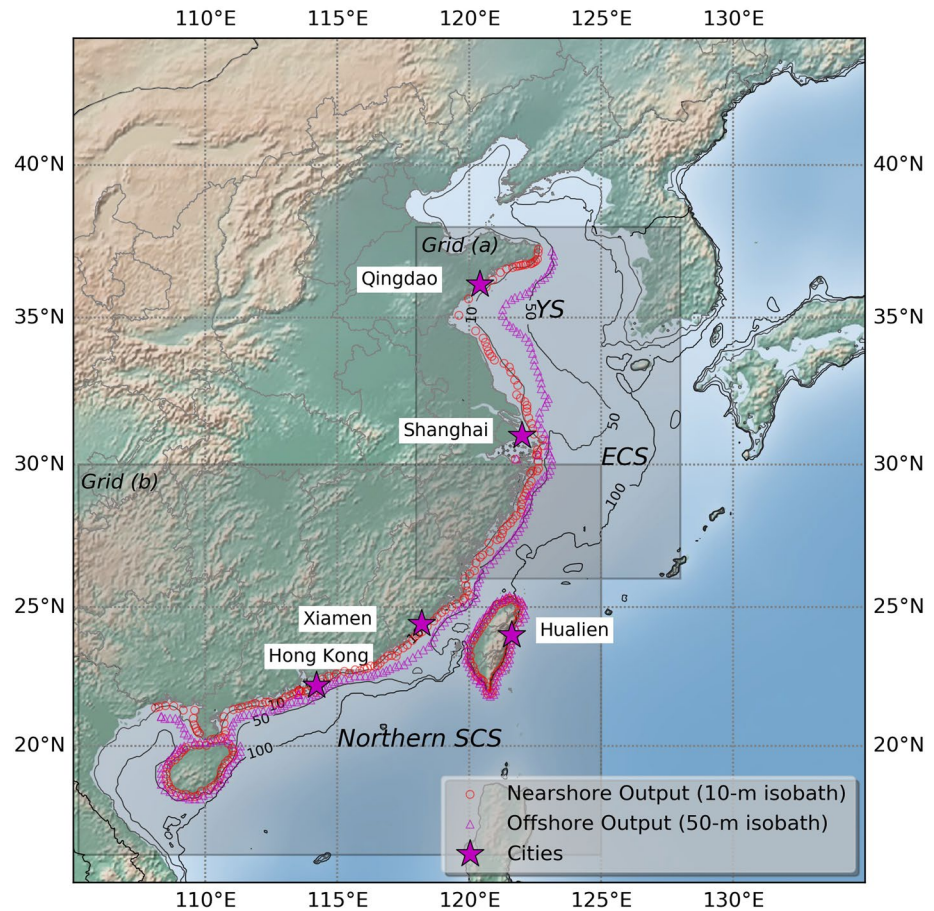
Figure 8. Offshore output points of tsunami propagation database (triangles), and nearshore output points (along the 10-m isobath) of FUNWAVE-TVD modeling (circles) along the coasts of Chinese Mainland and Taiwan Island with 10, 50, and 100 m bathymetric contours overlapped. The gray rectangles represent two modeling grids for FUNWAVE-TVD. Five coastal cities for hazard analysis are labeled with stars; These include Qingdao, Shanghai, Xiamen, Hong Kong, and Hualien.

As discussed in Section 3.1, the linear wave theory is only feasible for deep-water simulations (i.e., deeper than 50 m). It should not be used to model wave propagation over the shallow and broad shelf in the ECS, where the nonlinear effects and bottom friction are not negligible. It is also inappropriate to conduct offshore-to-nearshore wave-amplitude conversion using the Green's law derived from the linear wave theory. In Section 3.1, we have already defined an amplification/reduction factor K and obtained the K-value for each offshore point. With these K values, we can easily convert the offshore tsunami amplitudes to their nearshore counterparts along the 10-m isobath.

Due to the sparse observations of distant tsunamis along the ECS and SCS coasts, a coarse validation of our approach to derive the tsunami amplitudes along the 10-m isobath based on the propagation database and model-derived K values are summarized in Supporting Information Text S2 using five Pacific-wide events (Fujii et al., 2011; Selva & Marzocchi, 2004; Yu et al., 2011).

4.6.2. Boussinesq Modeling for Crustal Events

As previously discussed, a Boussinesq-type model is ideal to model the propagation of tsunamis generated by local crustal earthquakes beneath the continental shelves. We adopted the Boussinesq model FUN-WAVE-TVD to simulate wave dynamics with nonlinear effect, bottom friction, and dispersion effect (Kirby et al., 2013) for all the crustal events. Two computational domains were defined for the northern YS (26–
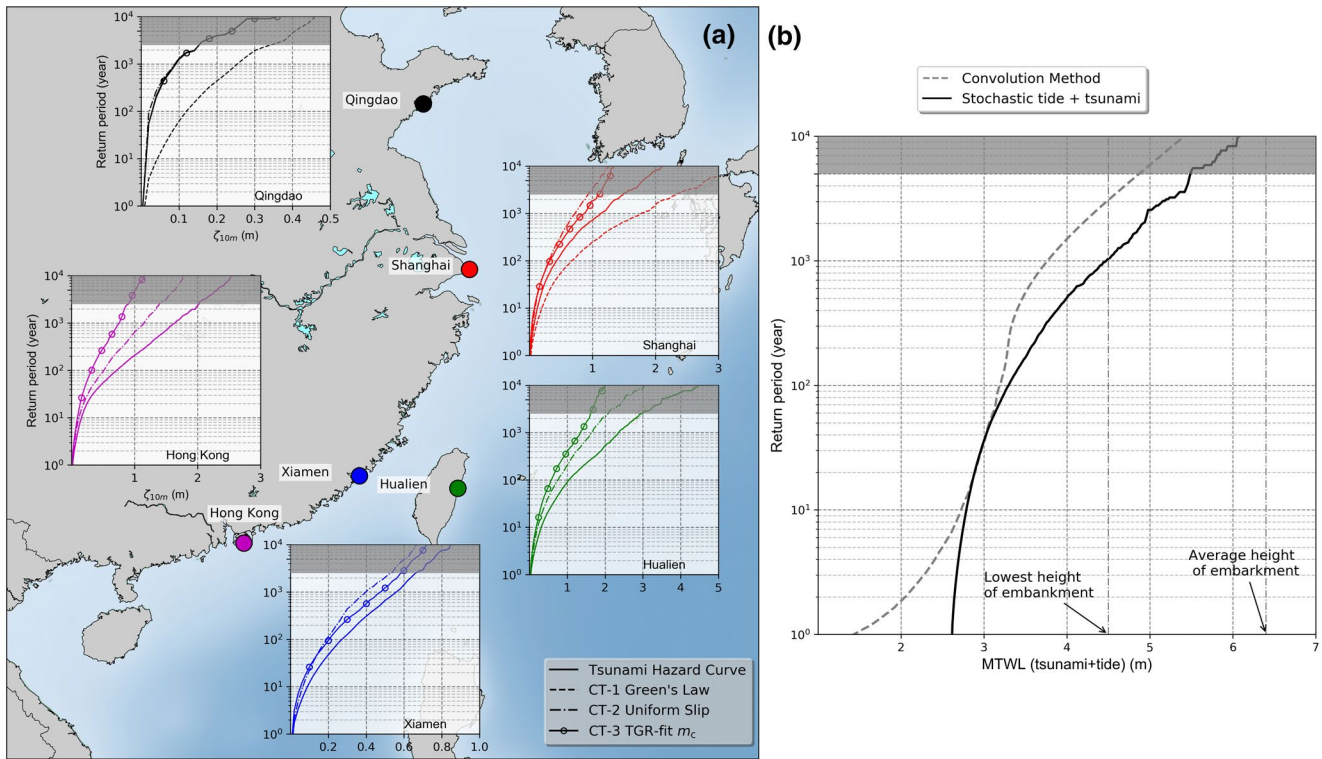
Figure 9. Left: Tsunami hazard curves for Qingdao, Shanghai, Xiamen, Hong Kong, and Hualien. Curves for the three control tests (Section 5.4) are plotted as dashed lines (PTHA using Green's law for offshore-to-nearshore conversion), dash-dotted lines (uniform coseismic slip), and solid lines with circles (smaller TGR-fit corner magnitude m_c for each subduction zones). Right: Hazard curves of Total Tsunami Water Level for Shanghai, China. The text annotation marks the lowest height of sea walls (4.5 m) along the coast of Pudong District, Shanghai. The shaded portion should be interpreted with caution due to lack of statistical significance. PTHA, Probabilistic Tsunami Hazard Assessment; TGR, tapered Gutenberg and Richter.

38°N and 118–128°E) and the northern SCS and TS (16–30°N and 105–125°E; Figure 8 grid a and b). Both grids have a resolution of 30-arc-sec resampled from the 15-arc-sec GEBCO-2019 Grid. FUNWAVE-TVD was rewritten with CUDA Fortran for GPU acceleration (Yuan et al., 2020). The nearshore output points along the 10-m isobath were extracted from the bathymetry grid (Figure 8). All 3,936 crustal events were simulated using FUNWAVE-GPU on 4 Nvidia V100 GPUs. Generally, the single-GPU version performs four to seven times faster than the original FUNWAVE-TVD does on a 36-core CPU node.

5. Results

5.1. Tsunami Hazard Curves

Tsunami hazard curves describe the annual probability of exceeding a range of tsunami amplitudes at points of interest along the coastlines. From north to south, we selected Qingdao, Shanghai, Xiamen, Hong Kong, and Hualien as representative points along the east coast of Chinese Mainland and Island of Taiwan. Hazard curves (solid lines) for these five sites are provided in Figure 9a. Return period, which is defined as the reciprocal of annual probability of exceedance, are used in the figure.

Here we use η_i to denote the nearshore maximum tsunami amplitude at the 10-m isobath for four different return periods (i = 50, 200, 500, 2,000 years). Hualien, located along the east coast of Taiwan Island, is exposed to the greatest hazard as it faces the Pacific Ocean without any sheltering. The η_{100} and η_{1000} values are ~1.05 m and 2.35 m, respectively. The hazard curve for Shanghai shows the η_{100} and η_{1000} values are 0.4–0.5 and 1.1–1.3 m, respectively. In the next century the probability of tsunami waves with amplitudes over 1 m to hit Shanghai is about 14%. For Hong Kong, this probability could rise to 40%. It should be mentioned that

the runup values could be larger than the 10 m-isobath values, which largely depend on the complexity of local topography and coastlines.

The maximum amplitude at the 2,000-year return period is a key index in Chinese Mainland for urban planning. The 2,000-year amplitude nearshore is 1.4 m in Shanghai, but is only 0.14 m at Qingdao along the northern coast of China (black dot). The tsunami hazards are negligible along the coastline of Shandong Peninsula, where the wide and shallow shelves in the ECS play a critical role in mitigating wave amplitudes from the transoceanic sources, especially those from the Nankai Trough and the Ryukyu Trench. Xiamen, located along the west coast of TS, benefits from the sheltering effect of the island of Taiwan, with a similarly a low level of tsunami hazard ($\eta_{2000} = 0.63$ m).

5.2. Hazard Curves of TTWL by Integrating Tidal Levels

In this study we define the TTWL along the coastline as a sum of tidal level and tsunami fluctuation. For shelves with moderate tsunami hazards and high tides, like the the shelf of the ECS, the probability of the TTWL exceeding a particular value is an important index for the design of coastal infrastructures (i.e., seawalls). The design crest elevation of seawalls along the coasts of China is determined by a combination of tidal level with 10% exceedance probability and other meteorological-related water levels (mainly storm surge and wind-wave runup) at different return periods. The main concern of policymakers is whether the existing coastal dykes are sufficiently high to resist the potential tsunami impact. In this section, we derive the hazard curves that take into consideration both the tides and the TWLs in Shanghai using two approaches. Presently, the coastlines of Shanghai are reinforced by high-standard seawalls to resist the extreme water level caused by typhoon-induced storm surge.

The hourly tides measured at the Luchao Port, Shanghai, from 2001 to 2019 are used to derive the discrete probability distributions at a discretized bin size of 0.1 m. The coast of Shanghai is mostly dominated by the semi-diurnal tide, with a mean tidal range of 2.6 m and a spring tidal range up to 5 m. To be more conservative, we use the Green's law to derive maximum tsunami amplitudes at 1-m isobaths from the 10-m isobaths nearshore of Shanghai.

For the first approach, we define the TTWL as $Z = \eta_{tide} + \eta_{tsu}$, assuming the tidal and tsunami levels are two independent variables and their probabilities can be described by some known discrete distributions. Considering z as an arbitrary water level, as shown in Equation 7, the probability of event $Z = z$ is the convolution of the probabilities of two pairwise independent events ($\eta_{tide} = k$) and ($\eta_{tsu} = z - k$), where k can be either the upper or the lower bound of Z.

$$P(Z = z) = \sum_{k=-\infty}^{\infty} P(\eta_{tide} = k) \cdot P(\eta_{tsu} = z - k) \tag{7}$$

We note that the TWL is small compared to the tidal level along the coastline of Shanghai. The cumulative probability of the TTWL exceeding a particular level z can then be approximated by Equation 8. The result is shown by the dashed line in Figure 9b.

$$P(Z \geq z) = \sum_{k \geq z}^{\infty} P(Z = k) \tag{8}$$

Compared to the first approach, the second approach seems to be more straightforward. The time series of a tsunami for a specific event can be characterized by an exponentially decaying fluctuation with the maximum amplitude occurring at the initial wave. The variation of the maximum tsunami amplitude can be expressed as a function of time t

$$\eta(t) = \eta_{max} \cdot exp\left(-\frac{\alpha t}{120}\right), \tag{9}$$

where $\alpha = 3.0$ is the decay constant, which is chosen by assuming the amplitude decays to an indistinguishable level (below 5%) within 120 h (Mofjeld et al., 2007; Satake et al., 2020). Supposing the initial tsunami wave arrives at a random tidal phase, the tidal time series can then be expressed as

$$\xi(t) = \sum_{i=1}^{I} H_i cos(\sigma_i t + p_i + p_{rand}),$$ (10)

where ξ is the tidal level, H_i and p_i are the tidal harmonic constants of amplitude and phase lag, respectively, I is the number of tidal constituents, and p_{rand} is the random tidal phase sampled between 0 and 2π. By summing up both the tsunami and tidal water level components, we have a catalog of TTWL time series for a total of 328,428 synthetic events for Shanghai. The aggregation of the TTWL catalog then gives the annual probability of TTWL above specific values, shown by the solid line in Figure 9b.

One can see these two approaches produce similar hazard curves of TTWL between return periods of 10 and 5,000 years. The 2,000-year TTWL is about 4.2–4.9 m, which is comparable to the lowest crest elevation of the seawalls (4.5 m) along the coast of Pudong District, Shanghai. Since the average crest elevation of the seawalls in this area is 6.4 m, we might expect relatively limited tsunami inundation hazards here due to the protection of the embankment.

5.3. Tsunami Hazard Maps and Source Deaggregation

A tsunami hazard map provides the maximum wave amplitude at an annual exceeding rate for every nearshore output point. As seen in Figure 10, the hazard maps for the return periods of 50, 200, 500, and 2,000 years clearly show the greatest tsunami hazards exist along the east coast of Taiwan Island. The 2,000-year maximum tsunami amplitude η_{2000} at the 10 m isobath there is above 3 m. The coastline of the south of Jiangsu province, Shanghai, the north of Zhejiang province, and the mouth of Pearl River in Guangdong (GD) province are generally exposed to moderate levels of tsunami hazards, with the η_{2000}-value ranging from 1.0 to 2.3 m. Tsunami amplitudes drop very quickly northward along the coasts of Jiangsu and Shandong provinces, and the η_{2000}-values barely exceed 0.3 m along the coast of Shandong. The tsunami hazards along the coast of TS are relatively low in comparison with those along the neighboring coastlines due to the sheltering effect of Taiwan Island.

As a whole, the distribution of tsunami hazards along the coastline of China demonstrates a pattern similar to the tidal observations during the 2011 Tohoku Tsunami in Figure 1. Figure 10 shows two segments of the coastlines with higher amplitudes at both flanks of the Yangtze Estuary, which supports findings of our ray tracing analysis described in Section 3.2.

As mentioned earlier, previous statements claimed that tsunami energy is dissipated by the wide continental shelves, and the tsunami hazards can be ignored along the coastline of China. Here, we show that those first-impression and qualitative statements were drawn from sparse, incomplete, and inaccurate historical records. The present study has, for the first time, quantitatively investigated the tsunami hazards along the east coast of Chinese Mainland based on a rigorous probabilistic approach. Our PTHA results suggest that the tsunami hazards along the coast of the ECS generated by far-field sources are moderate with the maximum tsunami amplitudes of 1–2 m. Considering the rapid growth of coastal population and economic activities in this area, the tsunami risks can certainly pose serious threats to the coasts and the probability of such an event should not be underestimated.

It is worth noting that tsunami hazards are noticeably higher at both flanks of the Yangtze Estuary in the ECS and the Pearl Estuary in the northern SCS, as suggested by the findings of the ray tracing study described in Section 3.2. To quantify the source contribution to the overall tsunami hazards for different exceedance wave amplitudes, we applied a deaggregation analysis to the PTHA results at Shanghai, Xiamen, Hong Kong, and Hualien. A deaggregated hazard map helps identify the main sources of the hazards at a target location. The deaggregated tsunami hazard maps for the exceedance wave amplitudes of 0.5, 1.0, 1.5, and 2.0 m are shown in Figure 11. The map only covers the subduction zones in the northwest Pacific Ocean. Other source zones present negligible hazards at above areas of interest except the Central Chile Trench.

Shanghai: The main source zones contributing to the tsunami hazards at Shanghai with the exceedance wave amplitude of 0.5 m include the Ryukyu Trench, the Nankai Trough, and Central Chile Trench. Other Northwest Pacific sources are also negligible. For the exceedance wave amplitude of 1.0 m, the majority of
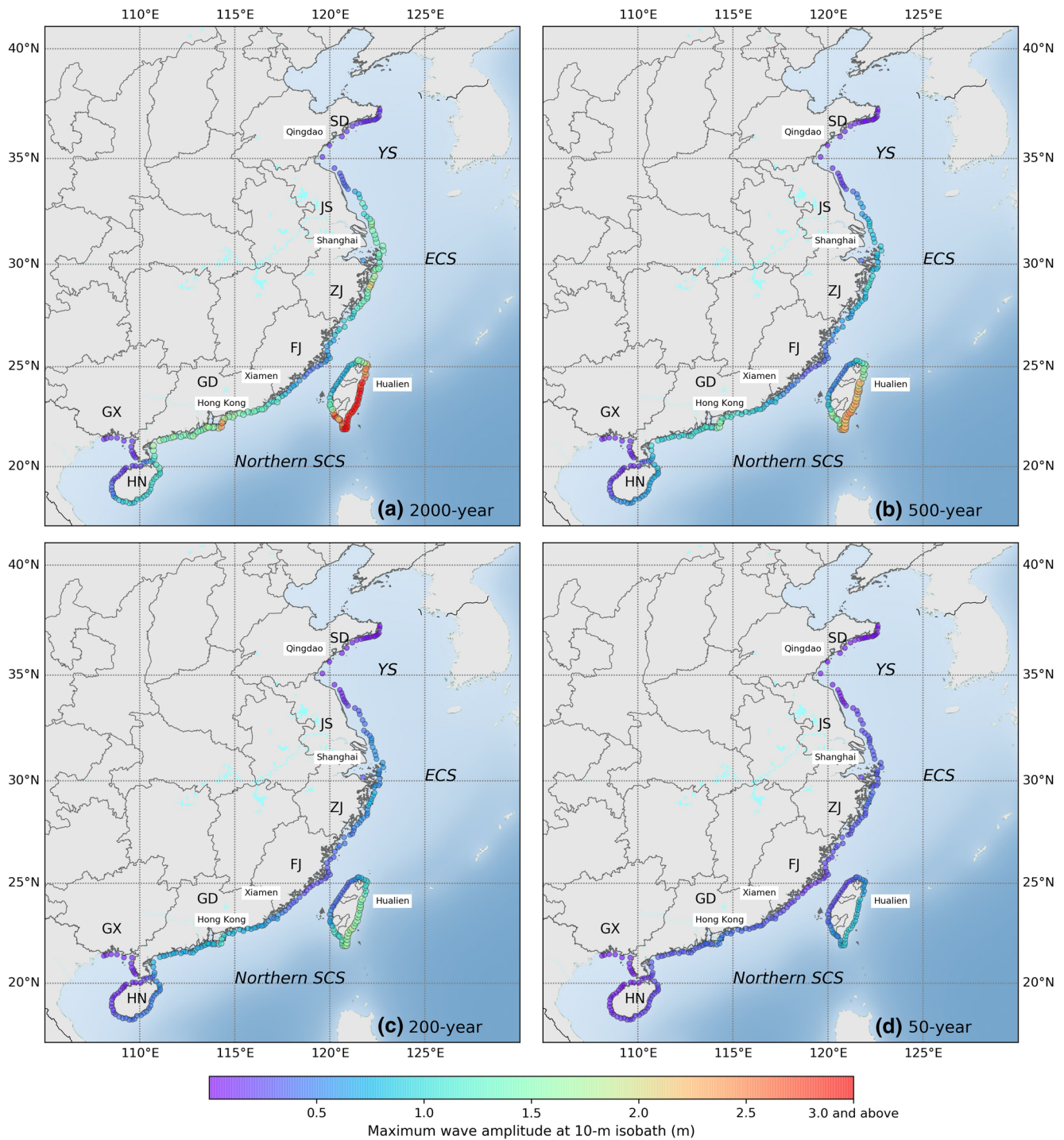
Figure 10. Maximum wave amplitude off the coasts of Chinese Mainland and Taiwan Island for return period of (a) 2,000 years, (b) 500 years, (c) 200 years, and (d) 50 years. Abbreviation: Yellow Sea (*YS*), East China Sea (*ECS*), South China Sea (*SCS*), Provinces of Shandong (SD), Jiangsu (JS), Zhejiang (ZJ), Fujian (FJ), Guangdong (GD), Guangxi (GX), Hainan (HN).

tsunami hazards comes from the Nankai Trough and the Ryukyu Trench. For events with wave amplitudes larger than 2 m, the contributing sources are predominantly from the Nankai Trough (75%), and the rest are from the Ryukyu Trench and the Izu-Boin Trench.
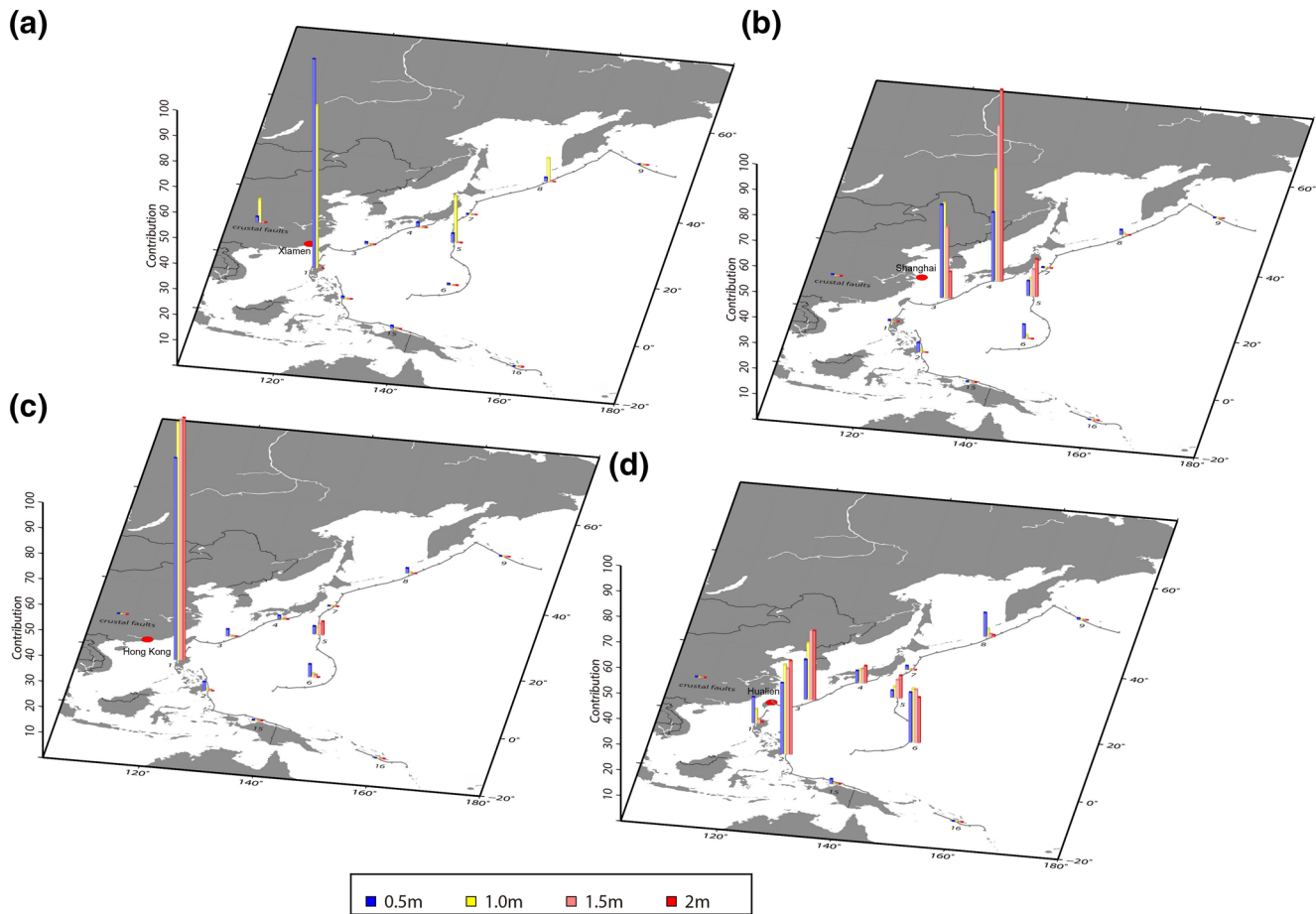
Figure 11. Geographic deaggregation of tsunami hazard for tsunami exceedance amplitude of 0.5 m, 1.0 m, 1.5 m, and 2.0 m at (a) Xiamen, (b) Shanghai, (c) Hong Kong, and (d) Hualien.

Xiamen: Xiamen is located at the south entrance of the TS. The vast majority of large-amplitude tsunami events are from the Manila Trench. However, the local seismic sources (crustal faults in the TS) contribute about 10% of tsunami events for wave amplitudes smaller than 1.0 m, and should not be neglected. On the other hand, the subduction zones in the Pacific produce only minor impact on Xiamen due to the wave sheltering effect of the Taiwan Island.

Hong Kong: The Manila Trench is the most dangerous source zone for Hong Kong in terms of potential tsunami hazards. Similar to Xiamen, Hong Kong is not susceptible to any of the circum-Pacific source zones. The main reason is the shallow and narrow Bashi Channel between Taiwan and Luzon (1,000 m) that protects the SCS from the impact of distant tsunamis.

Hualien: The composition of tsunami hazards for exceedance wave amplitudes of 0.5 and 1.0 m is more complicated, and the contributing sources cover most of subduction zones in the Pacific Ocean. However, the main threats for amplitudes greater than 2.0 m mainly come from, in a descending order, the Philippines Trough, the Ryukyu Trench, the Mariana Trench, the Izu-Bonin Trench, the Nankai Trough, and the Central Chile Trench (not shown in this map).

5.4. Sensitivity Analysis on Source Uncertainty and Hydrodynamic Modeling

PTHA study involves a multitude of uncertainties associated with the geophysical and geometric parameters that define the seismic sources, as well as the hydrodynamic modeling processes (i.e., governing equa-
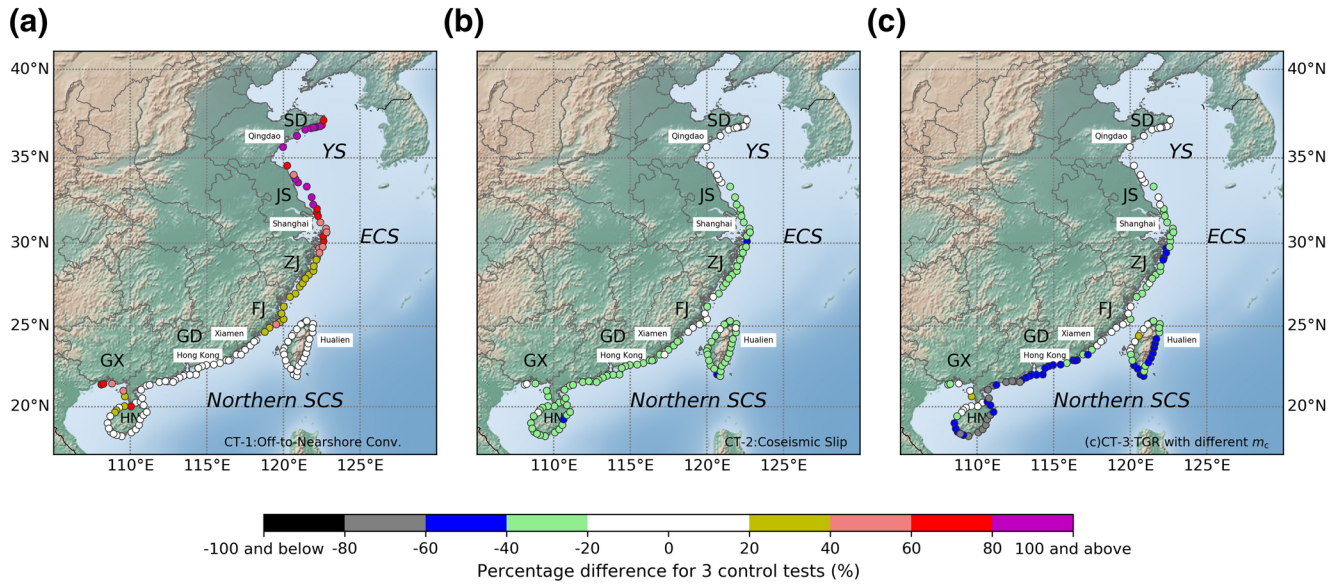
Figure 12. Percentage difference of tsunami hazard for the three control tests compared with the tsunami hazard maps in Section 5.2: PTHA using (a) the Green's law for offshore-to-nearshore conversion; (b) uniform coseismic slip, and (c) lower TGR-fit corner magnitude m_c. PTHA, Probabilistic Tsunami Hazard Assessment; TGR, tapered Gutenberg and Richter.

tions, grid resolution, the Green's law, and bathymetry). As introduced in Section 4, we incorporate our PTHA study with larger $m_{c,T}$-values computed from the seismic moment conservation principle, the heterogeneous slip model, and the hydrodynamic model-derived K-values for offshore-to-nearshore tsunami amplitude conversion. To demonstrate the sensitivity of tsunami hazard on these main uncertainties, three controlling tests are implemented to give the PTHA results based on the Green's law, the uniform slip distribution, and the TGR-fit m_c-values, respectively. The hazard curves of the three controlling tests for the five representative sites are overlapped in Figure 9a. In Figures 12a–12c, we present the results of the three controlling tests in terms of the spatial distribution of the percentage difference at all nearshore points relative to their 2,000-year tsunami amplitudes obtained in Section 5.1. The percentage difference is computed by

$$P_{diff} = \frac{\eta_{2000,CT-i} - \eta_{2000}}{\eta_{2000}}, \tag{11}$$

where the subscript $CT - i$ denotes the sequence number of the controlling tests.

Control test 1 (CT-1): The feasibility of Green's law over the wide and shallow shelves was discussed in Section 3.1, and a suite of Boussinesq model-derived K-values was derived. The first control test was carried out using the Green's law to convert the wave amplitudes from offshore to nearshore (Figure 12a). The $\eta_{2000,CT-1}$ values are considerably larger than η_{2000} along the coasts of the ECS and YS. In particular, the tsunami hazards along the coasts of the Shandong (SD) Province, the Jiangsu (JS) Province, Shanghai, and the Guangxi (GX) Province are overestimated by 40%–200%. The η_{2000} value for Shanghai is 1.4 m, which is almost 1 m smaller than $\eta_{2000,CT-1}$. The striking difference of tsunami amplitudes resulting from different hydrodynamic models over the broad continent shelf in the ECS highlights the significant uncertainties of tsunami modeling.

Control test 2 (CT-2): In this test we applied the uniform slip distribution in the PTHA. As one can see, the results are generally 20%–40% smaller than those based on heterogeneous slip distributions. The conclusion is in accordance with the findings of previous studies that the tsunami hazards tend to be underestimated by 20%–40% using uniform slip distributions (Li et al., 2016).

Control test 3 (CT-3): Variability of TGR relationship and associated corner magnitude m_c is one of the controlling sources of uncertainty. The two sets of corner magnitude listed in Table 1 (m_c and $m_{c,T}$) are used

to define the annual probability of earthquakes with different magnitudes in the Monte Carlo simulation. Here CT-3 is conducted by using a lower TGR-fit m_c-value. The uncertainty of the upper-limit magnitudes produces a significant reduction of the nearshore wave amplitudes by 20%–60% along the coasts of the Yangtze Estuary and the SCS. As discussed by many previous studies (Kagan & Jackson, 2013; McCaffrey, 2008; Rong et al., 2014), the large earthquakes that occurred in recent years were not surprises, and M 9 earthquakes can be expected in major subduction zones. In the present study, we use the principle of seismic moment conservation to circumvent the weaknesses of m_c estimates derived from earthquake catalog data alone.

6. Concluding Remarks

A PTHA study inspecting the earthquake/tsunami sources in both the circum-Pacific subduction zones and the local crustal faults has never been conducted along the coastline of China. Here, we present a PTHA study for the east coast of Chinese Mainland and the Taiwan Island based on the Monte Carlo simulation. Through source deaggregation, we investigated the roles of subduction zones around the Pacific Rim in the far field and the crustal earthquakes in the near field in terms of their contributions to the tsunami hazards at sites of interest. Moreover, we conducted some sensitivity analyses on several major uncertainties to examine how they affect the results of tsunami hazard levels.

Hydrodynamic modeling of tsunami wave propagation over the shallow and wide shelves is the main concern of the model-based PHTA study along the east coast of Chinese Mainland. We addressed this uncertainty using a Boussinesq model to account for the effects of nonlinearity, bottom dissipation, and frequency dispersion more accurately. We found that the simplified linear wave theory is not applicable to the PTHA study for the ECS, and overestimates the tsunami hazards there to a large extent.

We showed that wave focusing and scattering are the main drivers of the redistribution of tsunami energy across the continental shelf, which results in higher tsunami hazards on both flanks of the Yangtze Estuary. This finding was further confirmed and clearly illustrated by our ray tracing study performed along the tsunami propagating paths. In the northern part of the SCS, the main contributing source is Manila Trench, which could generate destructive tsunami waves on both flanks of the Pearl Estuary. Combining the PTHA and the ray tracing study, we were able to infer that the shallow tongue-shape bathymetric features at the mouths of the Yangtze River and the Pearl River Mouth can gradually alter the headings of tsunami energy rays and form energy focusing in the areas, and as a result amplify the TWLs in those areas. This conclusion challenges the traditional viewpoint that there is no tsunami risk along the coasts of East China. Although the majority of the coastlines are generally exposed to minor-to-moderate tsunami hazards, the bathymetric features may lead to uneven distribution of tsunami hazards along the coasts.

In addition, our PTHA fully considered the source complexity due to the heterogeneous nature of the rupture slips, and predicted a 20%–40% larger wave amplitude along the coasts of ECS and northern SCS.

We further examined the potential tsunami inundation along the coastline of Shanghai in terms of the TTWL by incorporating the aleatory uncertainty of the tidal level. The inundation risk is low as the TTWL at the return period of 2,000 years is considerably lower than the average crest elevation of seawalls at Pudong, Shanghai.

When comparing our results with other PTHA studies for the northern SCS, we found that large variability exists due to the parameters and geophysical processes used in different seismic and hydrodynamic models. Continued investigation is needed to further constrain these parameters through interdisciplinary efforts. Further quantification of uncertainties in large earthquake frequencies and the consequences for tsunami hazards is also recommended, noting the current study only considered uncertainties due to the corner-moment estimator.

It should be noted that the present study only considers seismic sources, while nonseismic sources, such as submarine landslides, are excluded. Although some recent numerical studies highlight the potential tsunamis generated by giant landslides from the north SCS shelf break (Li et al., 2019; Li et al., 2015), the lack of high-resolution bathymetry data sets and written records in this area makes the PTHA study of land-

slide-generated tsunamis impracticable. More collaborative efforts on hazard assessment of landslide-generated tsunamis in the ECS and SCS region are needed in the future.

Data Availability Statement

The random slip model to account for the complexity of the source are available at http://equake-rc.info/cers-software. The compiled earthquake catalogs for Chinese Mainland's offshore area and Pacific-wide subduction zones, the parameter file for unit sources of the subduction zones can be accessed via http://doi.org/10.5281/zenodo.4047714.

References

An, C., Liu, H., Ren, Z., & Yuan, Y. (2018). Prediction of tsunami waves by uniform slip models. *Journal of Geophysical Research: Oceans*, *123*(11), 8366–8382. https://doi.org/10.1029/2018JC014363

Ando, M., Kitamura, A., Tu, Y., Ohashi, Y., Imai, T., Nakamura, M., et al. (2018). Source of high tsunamis along the southernmost Ryukyu trench inferred from tsunami stratigraphy. *Tectonophysics*, *722*, 265–276. https://doi.org/10.1016/j.tecto.2017.11.007

Annaka, T., Satake, K., Sakakiyama, T., Yanagisawa, K., & Shuto, N. (2007). Logic-tree approach for probabilistic tsunami hazard analysis and its applications to the Japanese coasts. *Pure and Applied Geophysics*, *164*, 577–592.

Assatourians, K., & Atkinson, G. M. (2013). EqHaz: An open-source probabilistic seismic-hazard code based on the Monte Carlo simulation approach. *Seismological Research Letters*, *84*(3), 516–524. https://doi.org/10.1785/0220120102

Assatourians, K., & Atkinson, G. M. (2019). Implementation of a smoothed-seismicity algorithm in Monte Carlo PSHA software EqHaz and implications for localization of hazard in the western Canada sedimentary basin. *Seismological Research Letters*, *90*(3), 1407–1419. https://doi.org/10.1785/0220180284

Bird, P. (2003). An updated digital model of plate boundaries. *Geochemistry, Geophysics, Geosystems*, *4*, 1027. https://doi.org/10.1029/2001GC000252

Bird, P., & Kagan, Y. Y. (2004). Plate-tectonic analysis of shallow seismicity: Apparent boundary width, beta, corner magnitude, coupled lithosphere thickness, and coupling in seven tectonic settings. *Bulletin of the Seismological Society of America*, *94*(6), 2380–2399. https://doi.org/10.1785/0120030107

Blaser, L., Krüger, F., Ohrnberger, M., & Scherbaum, F. (2010). Scaling relations of earthquake source parameter estimates with special focus on subduction environment. *Bulletin of the Seismological Society of America*, *100*(6), 2914–2926. https://doi.org/10.1785/0120100111

Burbidge, D., Cummins, P. R., Mleczko, R., & Thio, H. K. (2008). A probabilistic tsunami hazard assessment for Western Australia. *Pure and Applied Geophysics*, *165*, 2059–2088.

Cheng, J., Rong, Y., Magistrale, H., Chen, G., & Xu, X. (2017). An M$_w$-based historical earthquake catalog for Mainland China. *Bulletin of the Seismological Society of America*, *107*(5), 2490–2500. https://doi.org/10.1785/0120170102

Christophersen, A., Litchfield, N., Berryman, K., Thomas, R., Basili, R., & Wallace, L., et al. (2015). Development of the Global Earthquake Model's neotectonic fault database. *Natural Hazards*, *79*(1), 111–135. https://doi.org/10.1007/s11069-015-1831-6

Davies, G. (2019). Tsunami variability from uncalibrated stochastic earthquake models: tests against deep ocean observations 2006–2016. *Geophysical Journal International*, *218*(3), 1939–1960. https://doi.org/10.1093/gji/ggz260

Davies, G., & Griffin, J. (2020). Sensitivity of probabilistic tsunami hazard assessment to far-field earthquake slip complexity and rigidity depth-dependence: Case study of Australia. *Pure and Applied Geophysics*, *177*, 1521–1548. https://doi.org/10.1007/s00024-019-02299-w

Davies, G., Griffin, J., Løvholt, F., Glimsdal, S., Harbitz, C., & Thio, H. K., et al. (2018). A global probabilistic tsunami hazard assessment from earthquake sources. *Geological Society, London, Special Publications*, *456*(1), 219–244.

Davies, G., Horspool, N., & Miller, V. (2015). Tsunami inundation from heterogeneous earthquake slip distributions: Evaluation of synthetic source models. *Journal of Geophysical Research: Solid Earth*, *120*(9), 6431–6451. https://doi.org/10.1002/2015JB012272

De Risi, R., & Goda, K. (2016). Probabilistic earthquake–tsunami multi-hazard analysis: Application to the Tohoku region, Japan. *Frontiers in Built Environment*, *2*, 25. https://doi.org/10.3389/fbuil.2016.00025

De Risi, R., Goda, K., Mori, N., & Yasuda, T. (2017). Bayesian tsunami fragility modeling considering input data uncertainty. *Stochastic Environmental Research and Risk Assessment*, *31*(5), 1253–1269. https://doi.org/10.1007/s00477-016-1230-x

Fujii, Y., Satake, K., Sakai, S., Shinohara, M., & Kanazawa, T. (2011). Tsunami source of the 2011 off the Pacific coast of Tohoku Earthquake. *Earth, Planets and Space*, *63*(7), 55. https://doi.org/10.5047/eps.2011.06.010

Geist, E. L., & Parsons, T. (2006). Probabilistic analysis of tsunami hazards. *Natural Hazards*, *37*(3), 277–314. https://doi.org/10.1007/s11069-005-4646-z

Geist, E. L., & Parsons, T. (2009). Assessment of source probabilities for potential tsunamis affecting the US Atlantic coast. *Marine Geology*, *264*(1–2), 98–108. https://doi.org/10.1016/j.margeo.2008.08.005

Gica, E., Teng, M. H., Liu, P. L.-F., Titov, V., & Zhou, H. (2007). Sensitivity analysis of source parameters for earthquake-generated distant tsunamis. *Journal of Waterway, Port, Coastal, and Ocean Engineering*, *133*(6), 429–441. https://doi.org/10.1061/(ASCE)0733-950X(2007)133:6(429)

Goda, K., Yasuda, T., Mai, P. M., Maruyama, T., & Mori, N. (2018). Tsunami simulations of mega-thrust earthquakes in the Nankai–Tonankai Trough (Japan) based on stochastic rupture scenarios. In Scourse, E. M., Wallis, S. R., Chapman, N. A., & Tappin, D. R. Tsunamis: Geology, hazards and risks (Vol. 456, p. 55–74). London, UK: Geological Society. https://doi.org/10.1144/SP456.1

González, F., Geist, E. L., Jaffe, B., Kânoğlu, U., Mofjeld, H., Synolakis, C., et al. (2009). Probabilistic tsunami hazard assessment at seaside, Oregon, for near-and far-field seismic sources. *Journal of Geophysical Research*, *114*(C11), C11023. https://doi.org/10.1029/2008JC005132

Grezio, A., Babeyko, A., Baptista, M. A., Behrens, J., Costa, A., Davies, G., et al. (2017). Probabilistic tsunami hazard analysis: Multiple sources and global applications. *Reviews of Geophysics*, *55*(4), 1158–1198. https://doi.org/10.1002/2017RG000579

Hayes, G. P., McNamara, D. E., Seidman, L., & Roger, J. (2014). Quantifying potential earthquake and tsunami hazard in the Lesser Antilles subduction zone of the Caribbean region. *Geophysical Journal International*, *196*(1), 510–521. https://doi.org/10.1093/gji/ggt385

Hayes, G. P., Moore, G. L., Portner, D. E., Hearne, M., Flamme, H., Furtney, M., & Smoczyk, G. M. (2018). Slab2, a comprehensive subduction zone geometry model. *Science*, *362*(6410), 58–61. https://doi.org/10.1126/science.aat4723

Heidarzadeh, M., & Kijko, A. (2011). A probabilistic tsunami hazard assessment for the Makran subduction zone at the northwestern Indian Ocean. *Natural Hazards*, *56*(3), 577–593. https://doi.org/10.1007/s11069-010-9574-x

Herrendörfer, R., Van Dinther, Y., Gerya, T., & Dalguer, L. A. (2015). Earthquake supercycle in subduction zones controlled by the width of the seismogenic zone. *Nature Geoscience*, *8*(6), 471–474. https://doi.org/10.1038/ngeo2427

Horspool, N., Pranantyo, I., Griffin, J., Latief, H., Natawidjaja, D., Kongko, W., et al. (2014). A probabilistic tsunami hazard assessment for Indonesia. *Natural Hazards and Earth System Sciences*, *14*(11), 3105. https://doi.org/10.5194/nhess-14-3105-2014

Hsu, Y.-J., Ando, M., Yu, S.-B., & Simons, M. (2012). The potential for a great earthquake along the southernmost Ryukyu subduction zone. *Geophysical Research Letters*, *39*(14), L14302. https://doi.org/10.1029/2012GL052764

Hsu, S.-K., Yeh, Y.-C., Sibuet, J.-C., Doo, W.-B., & Tsai, C.-H. (2013). A mega-splay fault system and tsunami hazard in the southern Ryukyu subduction zone. *Earth and Planetary Science Letters*, *362*, 99–107. https://doi.org/10.1016/j.epsl.2012.11.053

Hsu, Y.-J., Yu, S.-B., Loveless, J. P., Bacolcol, T., Solidum, R., Luis, A., Jr, et al. (2016). Interseismic deformation and moment deficit along the Manila subduction zone and the Philippine Fault system. *Journal of Geophysical Research: Solid Earth*, *121*(10), 7639–7665. https://doi.org/10.1002/2016JB013082

Ito, T., Yoshioka, S., & Miyazaki, S. (1999). Interplate coupling in southwest Japan deduced from inversion analysis of GPS data. *Physics of the Earth and Planetary Interiors*, *115*(1), 17–34. https://doi.org/10.1016/S0031-9201(99)00063-1

Kagan, Y. Y. (1997). Earthquake size distribution and earthquake insurance. *Communications in Statistics C: Stochastic Models*, *13*(4), 775–797. https://doi.org/10.1080/15326349708807451

Kagan, Y. Y., & Jackson, D. D. (2013). Tohoku earthquake: A surprise? *Bulletin of the Seismological Society of America*, *103*(2B), 1181–1194. https://doi.org/10.1785/0120120110

Kirby, J. T., Shi, F., Tehranirad, B., Harris, J. C., & Grilli, S. T. (2013). Dispersive tsunami waves in the ocean: Model equations and sensitivity to dispersion and Coriolis effects. *Ocean Modelling*, *62*, 39–55. https://doi.org/10.1016/j.ocemod.2012.11.009

Kreemer, C., Holt, W. E., & Haines, A. J. (2003). An integrated global model of present-day plate motions and plate boundary deformation. *Geophysical Journal International*, *154*(1), 8–34. https://doi.org/10.1046/j.1365-246X.2003.01917.x

Lane, E., Gillibrand, P., Wang, X., & Power, W. (2013). A probabilistic tsunami hazard study of the Auckland region, Part II: inundation modeling and hazard assessment. *Pure and Applied Geophysics*, *170*(9–10), 1635–1646. https://doi.org/10.1007/s00024-012-0538-9

Lau, A. Y. A., Switzer, A. D., Dominey, H. D., Aitchison, J. C., & Zong, Y. (2010). Written records of historical tsunamis in the northeastern South China Sea challenges associated with developing a new integrated database. *Natural Hazards and Earth System Sciences*, *10*(9), 1793–1806. https://doi.org/10.5194/nhess-10-1793-2010

Leonard, M. (2014). Self-consistent earthquake fault-scaling relations: Update and extension to stable continental strike-slip faults. *Bulletin of the Seismological Society of America*, *104*(6), 2953–2965. https://doi.org/10.1785/0120140087

LeVeque, R. J., Waagan, K., González, F. I., Rim, D., & Lin, G. (2016). Generating random earthquake events for probabilistic tsunami hazard assessment. *Pure and Applied Geophysics*, *173*, 3671–3692.

Li, L., Shi, F., Ma, G., & Qiu, Q. (2019). Tsunamigenic potential of the Baiyun slide complex in the South China Sea. *Journal of Geophysical Research: Solid Earth*, *124*(8), 7680–7698. https://doi.org/10.1029/2019JB018062

Li, L., Switzer, A. D., Chan, C.-H., Wang, Y., Weiss, R., & Qiu, Q. (2016). How heterogeneous coseismic slip affects regional probabilistic tsunami hazard assessment: A case study in the South China Sea. *Journal of Geophysical Research: Solid Earth*, *121*(8), 6250–6272. https://doi.org/10.1002/2016JB013111

Li, L., Switzer, A. D., Wang, Y., Weiss, R., Qiu, Q., Chan, C.-H., & Tapponnier, P. (2015). What caused the mysterious eighteenth century tsunami that struck the southwest Taiwan coast? *Geophysical Research Letters*, *42*(20), 8498–8506. https://doi.org/10.1002/2015GL065567

Li, H., Wang, Z., Yuan, Y., Xu, Z., Wang, P., & Shi, J. (2019). Probabilistic tsunami hazard assessment in the Bohai sea. *Acta Oceanologica Sinica*, *41*(01), 55–61. https://doi.org/10.3969/ji.ssn.0253-4193.2019.01.006

Li, H., Yuan, Y., Xu, Z., Wang, Z., Wang, J., Wang, P., et al. (2018). The dependency of probabilistic tsunami hazard assessment on magnitude limits of seismic sources in the South China Sea and adjoining basins. *Pure and Applied Geophysics*, *174*, 2351–2370.

Lin, J.-Y., Sibuet, J.-C., Hsu, S.-K., & Wu, W.-N. (2014). Could a Sumatra-like megathrust earthquake occur in the south Ryukyu subduction zone? *Earth, Planets and Space*, *66*(1), 49–57. https://doi.org/10.1186/1880-5981-66-49

Liu, L. (2001). Stable continental region earthquakes in South China. *Pure and Applied Geophysics*, *158*(9–10), 1583–1611. https://doi.org/10.1007/PL00001235

Løvholt, F., Glimsdal, S., Harbitz, C. B., Horspool, N., Smebye, H., De Bono, A., & Nadim, F. (2014). Global tsunami hazard and exposure due to large co-seismic slip. *International Journal of Disaster Risk Reduction*, *10*, 406–418. https://doi.org/10.1016/j.ijdrr.2014.04.003

Madsen, P. A., Fuhrman, D. R., & Schäffer, H. A. (2008). On the solitary wave paradigm for tsunamis. *Journal of Geophysical Research*, *113*(C12), C12012. https://doi.org/10.1029/2008JC004932

Mai, P. M., & Beroza, G. C. (2002). A spatial random field model to characterize complexity in earthquake slip. *Journal of Geophysical Research*, *107*(B11), 2308–2327. https://doi.org/10.1029/2001JB000588

McCaffrey, R. (2008). Global frequency of magnitude 9 earthquakes. *Geology*, *36*(3), 263–266. https://doi.org/10.1130/G24402A.1

Megawati, K., Shaw, F., Sieh, K., Huang, Z., Wu, T.-R., Lin, Y., et al. (2009). Tsunami hazard from the subduction megathrust of the South China Sea: Part i. source characterization and the resulting tsunami. *Journal of Asian Earth Sciences*, *36*(1), 13–20. https://doi.org/10.1016/j.jseaes.2008.11.012

Min, Z., Wu, G., Jiang, Z., Liu, C., & Yang, Y. (1995). *The catalogue of Chinese historical strong earthquakes*. Beijing, China: Seismological Press.

Mofjeld, H. O., González, F. I., Titov, V. V., Venturato, A. J., & Newman, J. C. (2007). Effects of tides on maximum tsunami wave heights: Probability distributions. *Journal of Atmospheric and Oceanic Technology*, *24*(1), 117–123. https://doi.org/10.1175/JTECH1955.1

Mori, N., Muhammad, A., Goda, K., Yasuda, T., & Ruiz-Angulo, A. (2017). Probabilistic tsunami hazard analysis of the Pacific coast of Mexico: Case study based on the 1995 Colima earthquake tsunami. *Frontiers in Built Environment*, *3*, 34–49. https://doi.org/10.3389/fbuil.2017.00034

Munk, W., O'Reilly, W., & Reid, J. (1988). Australia-Bermuda sound transmission experiment (1960) revisited. *Journal of Physical Oceanography*, *18*(12), 1876–1898. https://doi.org/10.1175/1520-0485

Nakamura, M., & Sunagawa, N. (2015). Activation of very low frequency earthquakes by slow slip events in the Ryukyu trench. *Geophysical Research Letters*, *42*(4), 1076–1082. https://doi.org/10.1002/2014GL062929

Namegaya, Y., & Satake, K. (2014). Reexamination of the A.D. 869 Jogan earthquake size from tsunami deposit distribution, simulated flow depth, and velocity. *Geophysical Research Letters*, *41*(7), 2297–2303. https://doi.org/10.1002/2013GL058678

Nguyen, P. H., Bui, Q. C., Vu, P. H., & Pham, T. T. (2014). Scenario-based tsunami hazard assessment for the coast of Vietnam from the Manila Trench source. *Physics of the Earth and Planetary Interiors*, *236*, 95–108. https://doi.org/10.1016/j.pepi.2014.07.003

Okada, Y. (1985). Surface deformation due to shear and tensile faults in a half-space. *Bulletin of the Seismological Society of America*, *75*(4), 1135–1154.

Okal, E. A., Synolakis, C. E., & Kalligeris, N. (2011). Tsunami simulations for regional sources in the South China and adjoining seas. *Pure and Applied Geophysics*, *168*(6–7), 1153–1173. https://doi.org/10.1007/s00024-010-0230-x

Omira, R., Baptista, M., & Matias, L. (2015). Probabilistic tsunami hazard in the Northeast Atlantic from near-and far-field tectonic sources. *Pure and Applied Geophysics*, *172*(3–4), 901–920. https://doi.org/10.1007/s00024-014-0949-x

Power, W., Wang, X., Lane, E., & Gillibrand, P. (2013). A probabilistic tsunami hazard study of the Auckland region, part I: propagation modeling and tsunami hazard assessment at the shoreline. *Pure and Applied Geophysics*, *170*(9–10), 1621–1634. https://doi.org/10.1007/s00024-012-0543-z

Qiu, Q., Li, L., Hsu, Y.-J., Wang, Y., Chung-Han, C., & Switzer, A. D. (2019). Revised earthquake sources along Manila trench for tsunami hazard assessment in the South China Sea. *Natural Hazards and Earth System Sciences*, *19*(7), 1565–1583. https://doi.org/10.5194/nhess-19-1565-2019

Ren, Y., Wen, R., Zhang, P., Yang, Z., Pan, R., & Li, X. (2017). Implications of local sources to probabilistic tsunami hazard analysis in south Chinese coastal area. *Journal of Earthquake and Tsunami*, *11*(01), 1740001. https://doi.org/10.1142/S1793431117400012

Rong, Y., Jackson, D. D., Magistrale, H., & Goldfinger, C. (2014). Magnitude limits of subduction zone earthquakes. *Bulletin of the Seismological Society of America*, *104*(5), 2359–2377. https://doi.org/10.1785/0120130287

Sandanbata, O., Watada, S., Satake, K., Fukao, Y., Sugioka, H., Ito, A., & Shiobara, H. (2018). Ray tracing for dispersive tsunamis and source amplitude estimation based on Green's law: Application to the 2015 volcanic tsunami earthquake near Torishima, south of Japan. *Pure and Applied Geophysics*, *175*(4), 1371–1385. https://doi.org/10.1007/s00024-017-1746-0

Satake, K. (2014). Advances in earthquake and tsunami sciences and disaster risk reduction since the 2004 Indian ocean tsunami. *Geoscience Letters*, *1*(1), 15. https://doi.org/10.1186/s40562-014-0015-7

Satake, K., & Atwater, B. F. (2007). Long-term perspectives on giant earthquakes and tsunamis at subduction zones. *Annual Review of Earth and Planetary Sciences*, *35*, 349–374. https://doi.org/10.1146/annurev.earth.35.031306.140302

Satake, K., Heidarzadeh, M., Quiroz, M., & Cienfuegos, R. (2020). History and features of trans-oceanic tsunamis and implications for paleo-tsunami studies. *Earth-Science Reviews*, *202*, 103112. https://doi.org/10.1016/j.earscirev.2020.103112.

Satake, K., & Tanioka, Y. (1999). Sources of tsunami and tsunamigenic earthquakes in subduction zones. *Pure and Applied Geophysics*, *154*(3–4), 467–483. https://doi.org/10.1007/s000240050240

Scala, A., Lorito, S., Romano, F., Murphy, S., Selva, J., Basili, R., et al. (2020). Effect of shallow slip amplification uncertainty on probabilistic tsunami hazard analysis in subduction zones: Use of long-term balanced stochastic slip models. *Pure and Applied Geophysics*, *177*, 1497–1520. https://doi.org/10.1007/s00024-019-02260-x

Scholz, C. H., & Campos, J. (2012). The seismic coupling of subduction zones revisited. *Journal of Geophysical Research*, *117*(B5), B05310. https://doi.org/10.1029/2011JB009003

Selva, J., & Marzocchi, W. (2004). Focal parameters, depth estimation, and plane selection of the worldwide shallow seismicity with Ms ≥ 7.0 for the period 1900–1976. *Geochemistry, Geophysics, Geosystems*, *5*(5), Q05005. https://doi.org/10.1029/2003GC000669

Selva, J., Tonini, R., Molinari, I., Tiberti, M. M., Romano, F., Grezio, A., et al. (2016). Quantification of source uncertainties in Seismic Probabilistic Tsunami Hazard Analysis (SPTHA). *Geophysical Journal International*, *205*(3), 1780–1803. https://doi.org/10.1093/gji/ggw107

Sepúlveda, I., Liu, P. L.-F., & Grigoriu, M. (2019). Probabilistic tsunami hazard assessment in South China Sea with consideration of uncertain earthquake characteristics. *Journal of Geophysical Research: Solid Earth*, *124*(1), 658–688. https://doi.org/10.1029/2018JB016620

Sepúlveda, I., Liu, P. L.-F., Grigoriu, M., & Pritchard, M. (2017). Tsunami hazard assessments with consideration of uncertain earthquake slip distribution and location. *Journal of Geophysical Research: Solid Earth*, *122*(9), 7252–7271. https://doi.org/10.1002/2017JB014430

Shan, D., Wang, P., Ren, Z., Sun, L., Zhao, L., & Fan, T. (2018). The Nankai Trough earthquake tsunami and its impacts on the Chinese coast of the East China. *Oceanologia et Limnologia Sinica*, *49*(6), 1151–1158. https://doi.org/10.11693/hyhz20180200038

Shi, F., Kirby, J. T., Harris, J. C., Geiman, J. D., & Grilli, S. T. (2012). A high-order adaptive time-stepping TVD solver for Boussinesq modeling of breaking waves and coastal inundation. *Ocean Modelling*, *43*, 36–51. https://doi.org/10.1016/j.ocemod.2011.12.004

Sieh, K., Natawidjaja, D. H., Meltzner, A. J., Shen, C.-C., Cheng, H., Li, K.-S., et al. (2008). Earthquake supercycles inferred from sea-level changes recorded in the corals of west Sumatra. *Science*, *322*(5908), 1674–1678. https://doi.org/10.1126/science.1163589

Sørensen, M. B., Spada, M., Babeyko, A., Wiemer, S., & Grünthal, G. (2012). Probabilistic tsunami hazard in the Mediterranean Sea. *Journal of Geophysical Research: Solid Earth*, *117*(B1), B01305. https://doi.org/10.1029/2010JB008169

Stirling, M., Goded, T., Berryman, K., & Litchfield, N. (2013). Selection of earthquake scaling relationships for seismic-hazard analysis. *Bulletin of the Seismological Society of America*, *103*(6), 2993–3011. https://doi.org/10.1785/0120130052

Storchak, D. A., Di Giacomo, D., Bondár, I., Engdahl, E. R., Harris, J., Lee, W. H., et al. (2013). Public release of the ISC–GEM global instrumental earthquake catalogue (1900–2009). *Seismological Research Letters*, *84*(5), 810–815. https://doi.org/10.1785/0220130034

Strasser, F. O., Arango, M., & Bommer, J. J. (2010). Scaling of the source dimensions of interface and intraslab subduction-zone earthquakes with moment magnitude. *Seismological Research Letters*, *81*(6), 941–950. https://doi.org/10.1785/gssrl.81.6.941

Suppasri, A., Imamura, F., & Koshimura, S. (2012). Tsunami hazard and casualty estimation in a coastal area that neighbors the Indian Ocean and South China Sea. *Journal of Earthquake and Tsunami*, *6*(02), 1250010. https://doi.org/10.1142/S1793431112500108

Synolakis, C. E. (1991). Green's law and the evolution of solitary waves. *Physics of Fluids A: Fluid Dynamics*, *3*(3), 490–491. https://doi.org/10.1063/1.858107

Tang, L., Titov, V., Wei, Y., Mofjeld, H., Spillane, M., Arcas, D., et al. (2008). Tsunami forecast analysis for the May 2006 Tonga tsunami. *Journal of Geophysical Research*, *113*, C12015. https://doi.org/10.1029/2008JC004922.

Titov, V. V., Gonzalez, F. I., Bernard, E., Eble, M. C., Mofjeld, H. O., Newman, J. C., & Venturato, A. J. (2005). Real-time tsunami forecasting: Challenges and solutions. *Natural Hazards*, *35*(1), 35–41. https://doi.org/10.1007/s11069-004-2403-3

Wang, K., & Bilek, S. L. (2014). Fault creep caused by subduction of rough seafloor relief. *Tectonophysics*, *610*, 1–24. https://doi.org/10.1016/j.tecto.2013.11.024

Wang, X., & Liu, P. L.-F. (2006). An analysis of 2004 Sumatra earthquake fault plane mechanisms and Indian Ocean tsunami. *Journal of Hydraulic Research*, *44*(2), 147–154. https://doi.org/10.1080/00221686.2006.9521671

Wang, S., Wu, G., & Shi, Z. (1999). *The catalogue of recent earthquakes in China (AD 1912–AD 1990)*. Beijing, China: China Science and Technology Publishing House.

Wei, Y., Chamberlin, C., Titov, V. V., Tang, L., & Bernard, E. N. (2013). Modeling of the 2011 Japan tsunami: Lessons for near-field forecast. *Pure and Applied Geophysics*, *170*(6–8), 1309–1331. https://doi.org/10.1007/s00024-012-0519-z

Wei, Y., Newman, A. V., Hayes, G. P., Titov, V. V., & Tang, L. (2014). Tsunami forecast by joint inversion of real-time tsunami waveforms and seismic or gps data: Application to the Tohoku 2011 tsunami. *Pure and Applied Geophysics*, *171*(12), 3281–3305. https://doi.org/10.1007/s00024-014-0777-z

Wu, T.-R., & Huang, H.-C. (2009). Modeling tsunami hazards from Manila trench to Taiwan. *Journal of Asian Earth Sciences*, *36*(1), 21–28. https://doi.org/10.1016/j.jseaes.2008.12.006

Yu, F., Wang, P., Zhao, L., & Yuan, Y. (2011). Numerical simulation of 2010 Chile tsunami and its impact on Chinese coasts. *Chinese Journal of Geophysics*, *54*(4), 918–925. https://doi.org/10.3969/j.issn.0001-5733.2011.04.005

Yu, F., Yuan, Y., Zhao, L., & Wang, P. (2011). Evaluation of potential hazards from teletsunami in China: Tidal observations of a teletsunami generated by the Chile m 8.8 earthquake. *Chinese Science Bulletin*, *56*(11), 1108–1116.

Yuan, Y., Shi, F., Kirby, J. T., & Yu, F. (2020). FUNWAVE-GPU: Multiple-GPU acceleration of a Boussinesq-type wave model. *Journal of Advances in Modeling Earth Systems*, *12*(5), e2019MS001957. https://doi.org/10.1029/2019MS001957

Zamora, N., & Babeyko, A. Y. (2019). Probabilistic tsunami hazard assessment for local and regional seismic sources along the pacific coast of Central America with emphasis on the role of selected uncertainties. *Pure and Applied Geophysics*, *177*, 1471–1495. https://doi.org/10.1007/s00024-019-02372-4

Zhao, X., Liu, H., & Wang, B. (2016). Tsunami waveforms and runup of undular bores in coastal waters. *Journal of Engineering Mechanics*, *142*(7), 06016003. https://doi.org/10.1061/(ASCE)EM.1943-7889.0001086

Zöller, G. (2013). Convergence of the frequency-magnitude distribution of global earthquakes: Maybe in 200 years. *Geophysical Research Letters*, *40*(15), 3873–3877. https://doi.org/10.1002/grl.50779